Morphological wave attenuation of the nature-based flood defense: A case study from Chongming Dongtan Shoal, China

Jie Mi [a], Min Zhang [a,*], Zhenchang Zhu [b], Vincent Vuik [c], Jiahong Wen [a], Hongkai Gao [d], Tjeerd J. Bouma [e]

[a] School of Environmental and Geographical Sciences, Shanghai Normal University, Shanghai 200234, China
[b] Guangdong Provincial Key Laboratory of Water Quality Improvement and Ecological Restoration for Watersheds, Institute of Environmental and Ecological Engineering, Guangdong University of Technology, Guangzhou, China
[c] Delft University of Technology, Faculty of Civil Engineering and Geosciences, P.O. Box 5048, 2600 GA Delft, the Netherlands
[d] School of Geographical Sciences, East China Normal University, Shanghai 200241, China
[e] Department of Estuarine and Delta Systems, Royal Netherlands Institute for Sea Research and Utrecht University, Yerseke, the Netherlands

HIGHLIGHTS

- Saltmarsh morphology is key to reducing the uncertainty of Nature-based Flood Defense.
- Major wave attenuation by over 2/3th is from the saltmarsh morphology.
- Submerged breakwater is cost-effective on wave mitigation and fostering saltmarshes.

GRAPHICAL ABSTRACT
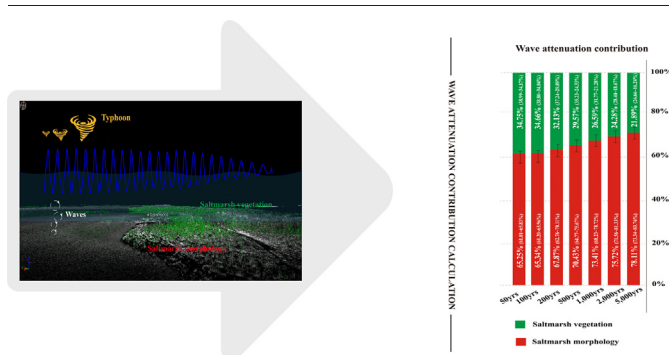
ARTICLE INFO

ABSTRACT

The risk of coastal storm flooding is deteriorating under global warming, especially for the heavily urbanized deltaic cities, like Shanghai. The Nature-Based Flood Defense (NBFD), as an eco-friendly design alternative for hard infrastructure against coastal flooding, is gaining attention. Nevertheless, the vulnerability of saltmarsh due to the biological instability, resulting in the uncertainties on coastal protection, is considered the bottleneck challenge that hinders the broad application of the NBFD concept. We argue that except for direct wave attenuations by the above-ground vegetation during storms, the gradual sediment trapping and consolidating during the non-storm period is a more crucial function of coastal saltmarsh, which mitigates storm waves by forming a broader and higher intertidal morphology. This benefit is an important value of saltmarsh-based coastal protection but is largely neglected in many NBFD studies. Taking Chongming Dongtan Shoal (CDS) as a case study, we demonstrated that over 2/3th wave attenuation during storms is contributed by the saltmarsh morphology, and less than 1/3th is from the saltmarsh vegetation. The relative contribution of the saltmarsh morphology on wave mitigation is even enhanced under the increasing storm grades from 100 yrs. to 5000 yrs. return levels. To promote this idea for broader application, the cost-benefit analysis of three artificial NBFD solutions (e.g., submerged breakwater, timber piles, and sand nourishment) are compared. We identified an optimal measure of the submerged breakwater for CDS, which minimizes the ecological impact and maximizes the cost-benefit. Moreover, the wave-free zone behind the breakwater increases the chance of vegetation establishment, helps suspended sediment trapping, hence fostering a beneficent cycle for saltmarsh restoration. In summary, ignoring the contribution of saltmarsh morphology on wave attenuation largely underestimated the benefits of vegetation-based coastal protection, which should be greatly emphasized to provide a solid basis for developing NBFD.

* Corresponding author.
E-mail address: zhangmin@shnu.edu.cn (M. Zhang).

1. Introduction

Global intensifying storms are extremely dangerous for coastal safety (Hallegatte et al., 2013; Temmerman et al., 2013; Schuerch et al., 2019). The heavily urbanized coastal community (Temmerman et al., 2013) accelerates the land subsidence (Syvitski et al., 2009), combined with climate change (Oppenheimer et al., 2019) collectively induce the risk of future coastal flooding. Except for hard coastal seawalls and other adaption measures (e.g., dikes, sluice gates, and breakwaters), there is a growing need to build sustainable coastal defense using nature-based solutions (Temmerman et al., 2013). Accordingly, some low-lying countries and regions, such as the Netherlands and Mississippi River Delta in the United States, have reached a consensus to build nature-based flood defense (NBFD) for coastal protection (Temmerman et al., 2013; Bouma et al., 2014). However, the uncertainty of wetlands on coastal protection, particularly the vulnerability of saltmarsh vegetation under extreme storm impacts, remains largely unknown (Temmerman et al., 2013; Bouma et al., 2014; Vuik et al., 2018a).

An important uncertainty of NBFD is mainly due to the vulnerability of plants that the above-ground structure is fragile (Vuik et al., 2018a, 2018b). Which means the reliability of vegetation on storm defense is limited by a threshold that varies following the seasonal phenological characteristics (Bouma et al., 2014; Vuik et al., 2018). Such a threshold effect is even amplified under simultaneous or consecutive strikes of storms since the global storm hazards are very likely increasing in the future under climate changes (Wu et al., 2022). It is widely recognized that nearshore wave energy dissipation mainly includes three processes: roughness bottom friction, vegetation bulk drag force, and depth-induced wave breaking (Möller and Spencer, 2002). Many studies evaluating the effectiveness of saltmarsh-based flood defense focused on the combined effect of vegetation bulk drag force and bottom frictions, i.e., through the enhanced bottom friction by validation (Baron-Hyppolite et al., 2019; Garzon et al., 2019; Chong et al., 2021). In contrast, the role of depth-induced wave breaking was not well studied in NBFD, which is actually significant, especially during severe storms when the foreshore is submerged and the stems are broken (Leonardi et al., 2018). Such a knowledge gap limits the value of saltmarsh morphology on coastal protection to be explored deeply. We argue that the depth-induced wave breaking by saltmarsh morphology protecting the coastline can be treated as the "recumbent seawall", which is based on the solid physical law of breaking wave height to water depth ratio (Vuik et al., 2016), hence has the potential to reduce the uncertainty of NBFD under strikes of storms.

It is well known that coastal wave reduction is positively correlated with the foreshore width (Zhu et al., 2020; Willemsen et al., 2020). The function of vegetated foreshores on wave attenuation has been observed and modelled even during storm conditions (Vuik et al.,2016; Chong et al., 2021). The vegetation attached to the tidal flat also protects the foreshore morphology from erosion by preventing intense wave breaking (Vuik et al., 2016; Willemsen et al., 2020). However, the value of saltmarsh morphology on wave attenuation is underestimated in many studies, and that of saltmarsh vegetation is overestimated for NBFD. Actually, some coastal restoration works are using the function of intertidal morphology for coastal protection (Reed et al., 2018), such as the engineering of sand nourishment derived from nearshore dredging (Vuik et al., 2019), but the unconsolidated sediments sprayed on exposed foreshores are quickly taken away by the longshore current (Zhou et al., 2016; Leonardi et al., 2018). Unlike sand nourishment, the positive feedback of sediment deposition, trapping by saltmarsh, and roots expansion of vegetation, help to consolidate the deposition (Spencer et al., 2016; Leonardi et al., 2018), consequently creating a more stable sedimentary layer. The interaction of saltmarsh and highly turbid water can continuously establish a new equilibrium profile (Kirwan et al., 2016). In addition, vegetated foreshores can recover quickly after each storm impact by constantly trapping suspended sediments (Duarte et al., 2013; Schuerch et al., 2019).

Coastal saltmarshes will not drown under global warming according to many ecologists (Duarte et al., 2013; Kirwan et al., 2016; Schuerch et al., 2019). The vegetated foreshores will keep pace with the sea-level rise in the accretional estuaries and coastlines. However, the self-adapting capacity of saltmarsh was neglected until the 1970s (Kirwan et al., 2016). Similarly, the flood protection function of saltmarsh morphology has not been paid enough attention since NBFD was first proposed in 2013 (Temmerman et al., 2013). Research works such as Möller et al. (2014), Vuik et al. (2016), and Willemsen et al. (2020) had mentioned the importance of the elevated saltmarsh platform and studied the combined tidal flat and saltmarsh on wave energy dissipation. Here, we explicitly evaluated the relative importance of saltmarsh morphology versus saltmarsh vegetation on the contribution of wave attenuation. The storm wave mitigations by saltmarsh vegetation and morphology have been studied in the temperate zone, e.g., the Dutch estuaries (Vuik et al., 2016; Willemsen et al., 2020). We aim to study the function of saltmarsh morphology as a compensation for the uncertainty of saltmarsh vegetation-based NBFD in the subtropical zone near the mouth of the Yangtze River, where typhoons are frequent and suspended sediment concentrations (SSCs) are among the highest in the world.

The focus of this paper is to answer: Can the saltmarsh morphology make up for the instability of saltmarsh vegetation, thereby reducing the uncertainty of NBFD on coastal protection in the face of rising sea levels and intensifying storms? If so, how to apply the concept of morphological wave mitigation in NBFD? Based on numerical simulations, we discerned the relative contributions of saltmarsh morphology versus saltmarsh vegetation on wave attenuation under designed storm wave conditions and quantified the cost-effectiveness of morphology-based NBFD measures for coastal restorations. We further tested the sensitivity of vegetation setting (e.g., single and mixed vegetations) and vegetation modelling (e.g., implicit and explicit vegetation modelling) approaches on wave energy dissipation. Finally, the cost-benefit of natural and artificial restoration works, such as sand nourishment, submerged breakwater, and timber piles, were evaluated, attempting to provide a reference for broader NBFD applications. A reliable hybrid NBFD solution has the potential to restore the heavily urbanized coastline is lacking so far, which could promote the more widespread implementation of nature-based flood mitigation programs into policy for sustainable coastal management.

2. Study area

Chongming Island, located at the mouth of the Yangtze River, is among the largest alluvial islands in the world. We focus on the eastern edge of Chongming Island, named the Chongming Dongtan Shoal (CDS) wetland, which is exposed to strong storm impact from the East China Sea (Fig. 1). The wide intertidal area is approximately 5.1 km wide from north to south and 10.8 km long from east to west, covering an area of roughly $42 km^2$ (31°26′ ~ 31°37′N, 121°46′ ~ 122°02′E). It is an essential stop for the international waterfowl migrating in the Australia-Asia-Siberia region (Ma et al., 2004). Tidal channels meandering through densely covered saltmarsh are observable from the stereo landscape (Fig. 1). Plant communities of high marsh, middle marsh, and low marsh are divided according to land elevation and saltwater inundation frequency (Fig. 1). After the 2013 reclamation of CDS, the invasive species of *Spartina alterniflora* was almost removed by blocking the northern part of the wetland from the sea (Hu et al., 2015). Currently, the three dominant species occupying the southern part of CDS follow a distribution pattern of a diatom on the bare flat-*Scirpus mariqueter-Phragmites australis* (Chong et al., 2021).

CDS wetland is profoundly influenced by the tide from the sea and river from upstream of the Yangtze. High sediment supplies with suspended sediment concentrations of 0.1-1 kg/m^3 were measured at Datong Station (Dai et al., 2018). From which about half was deposited in the estuary area, providing a rich sediment source for the saltmarsh morphology (Liu et al., 2010; Dai et al., 2016a, 2016b), with fine sand and mud accounting for over 90% (Dai et al., 2016). The astronomical tide influencing the area is irregular semi-diurnal tide with a cycle of
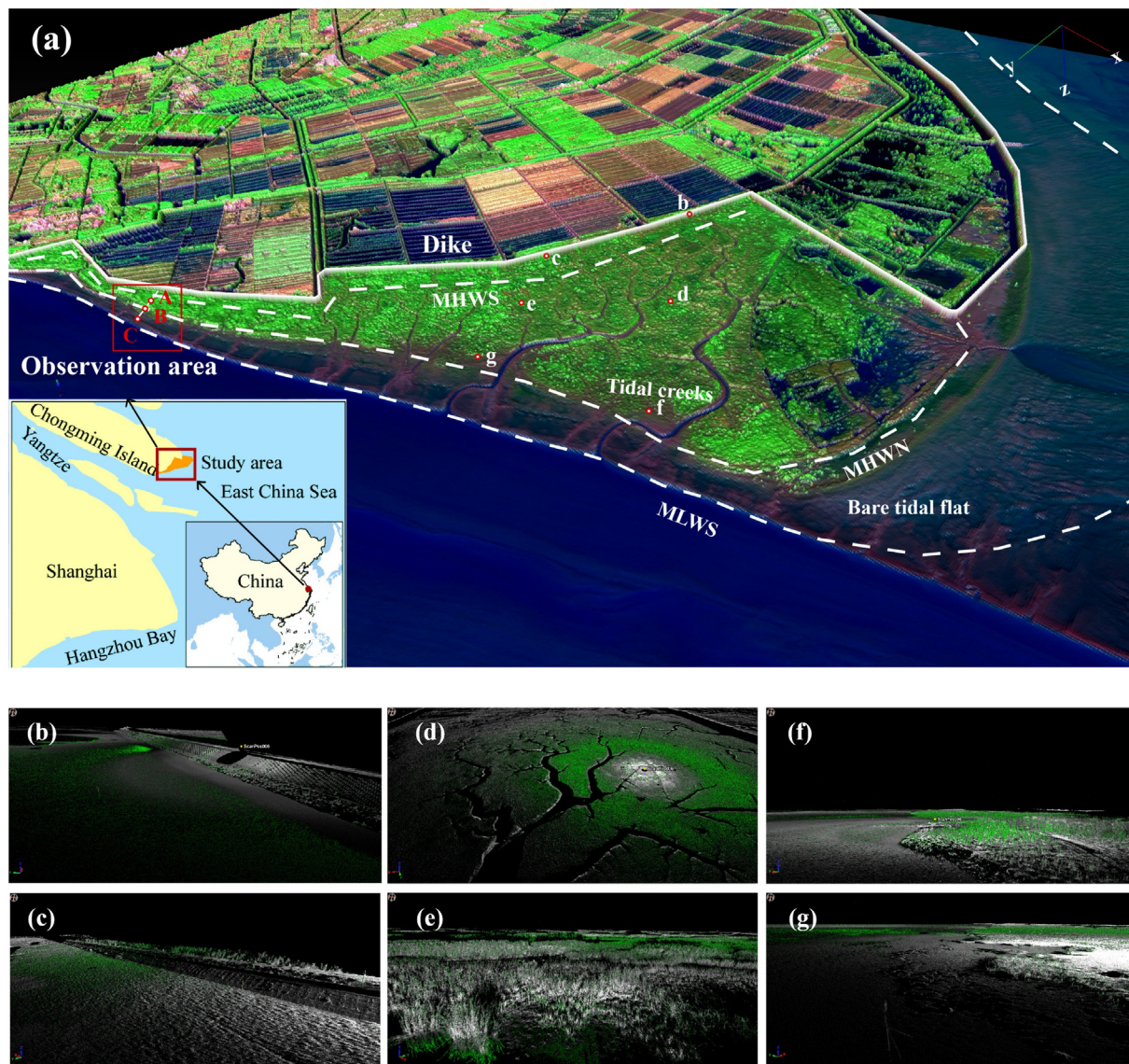
Fig. 1. Stereo-pair images retrieval of (a) the saltmarsh morphology and saltmarsh vegetation distribution on Chongming Dongtan Shoal (CDS) wetland, obtained from aerial photogrammetry detecting located on the eastern edge of Chongming Island in Yangtze Estuary. Examples of saltmarsh detection by RIEGL 3D laser scanner for (b,c) high marsh, (d,e) middle marshes, and (f,g) low marsh and bare tidal flat.

about 12 h and 24 min - a total of ~760 high-low tides over the year (Gao, 2020). The nearshore tidal range is 2.6 m on average and 3.5 m during spring tides (Dai et al., 2016a, 2016b). The deepest wave penetrating limit is up to -6 m below sea level, which is defined as the seaward boundary of CDS wetland.

The most devastating feature of CDS is the frequent impacts of typhoons from the Northwest Pacific, causing damage to the saltmarsh every five to ten years (e.g., Typhoon "Babe" in 1977, Typhoon "Winnie" in 1997, Typhoon "Lekima" in 2019, .etc). Historically, the maximum wind speed measured at Sheshan station (~20 km east of CDS) during typhoons can reach 32.6 m/s, with storm surges up to 2 m and significant wave heights (SWHs) up to 3.5–5 m (Chong et al., 2021). Under the dominant waves and currents, the south part of CDS experienced erosion recently, the eastern shoal was transitioning from fast accretion to a slow regression, and the northern shoal was still in the process of rapid accretion (Gao, 2020). To prevent possible future large-scale erosion due to dramatic sediment supply decrease (Dai et al., 2016a, 2016b) and typhoon impacts (Schuerch et al., 2019), the saltmarsh beyond the seawall should be protected by forming a high and sizeable intertidal zone (Vuik et al., 2019).

3. Material and methods

3.1. Data acquisition

The data used in setting the numerical model primarily obtained from field observations and reanalysis data (Fig. 2). The field observations included four sources, e.g., field landscape detecting, field wave observation, archived hydrologic station data collecting, and satellite remote sensing data collecting.

The saltmarsh morphology and saltmarsh vegetation were obtained from a unique in-situ observations of CDS in August and December 2017, detecting using UAV (Phantom4RTK) aerial photogrammetry with a spatial resolution of 0.5 m (Fig. 1a). The vegetation coverage height was obtained by subtracting the summer DSM (Digital Surface Model) to the winter DSM corrected by a vegetation filtering algorithm (Yilmaz et al., 2018). The vertical accuracy of DEM (Digital Elevation Model) covering CDS was estimated to be 0.1 m. Outside CDS, i.e., the large neighboring bathymetries of the Yangtze Estuary and mouth bar area, was defined using 2005, 2007, and 2008 navigation charts provided by the Maritime Survey Bureau of Shanghai (Zhang et al., 2016). A further outer area surrounding the
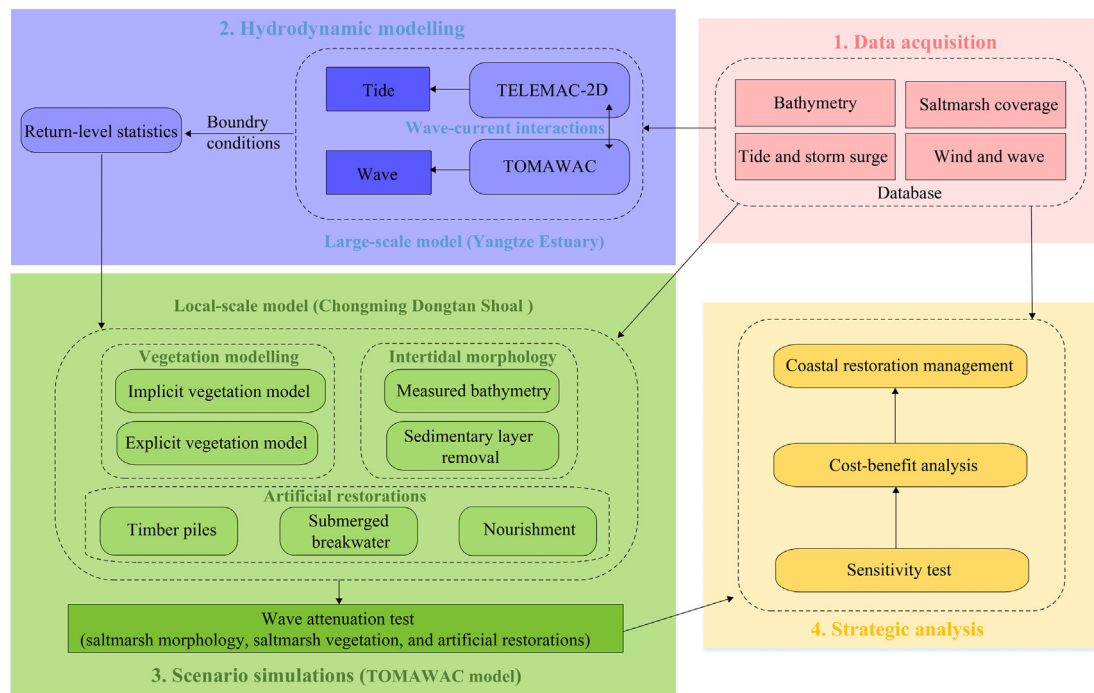
Fig. 2. A flowchart summarizing the methodology. Two sets of hydrodynamic models, including a large-scale Yangtze Estuary model, were connected to the small-scale Chongming Dongtan Shoal (CDS) model to test the effectiveness of saltmarsh morphology versus saltmarsh vegetation on storm wave attenuation. Round boxes represent models or calculations; square boxes represent datasets.

Hangzhou Bay and the continental shelf area was supplemented by the General Bathymetric Chart of the Oceans (http://www.gebco.net) with a spatial resolution of 30 m × 30 m. These bathymetry data from different sources were with different datums; hence all depth points (in ESRI shapefile data format converted from DEMs) were converted relative to the Huanghai1985 datum and reprojected to UTM Zone 51 N before a careful mosaic in ArcGIS10.6 (https://www.esri.com/en-us/home). Finally, the high-resolution depth information of CDS and coarser nearby depth information were used for the bathymetry boundary of the local-scale model and large-scale model, respectively (Fig. 2).

The meteorological and hydrological data were collected to drive the model as boundary conditions. The meteorological wind data to drive the water-air interface boundary were obtained from the reanalysis data of ECMWF (European Centre for Medium-Range Weather Forecasts), which were subject to a suite of data quality control and data selection procedures before being made available at https://www.ecmwf.int (Dee et al., 2011). The wind field at 10 m height was imposed over a vast ocean area in the large-scale model (Fig. 3a) with a temporal resolution of 6 h and spatial resolution of 12.5 km, respectively. The seaward boundary was driven by tidal amplitude and tidal velocity provided by TPXO7.2 (the global ocean tidal model). The TPXO7.2 database is a current version of the global model of ocean tides, which best fits, in a least-squares sense, the Laplace Tidal Equations and along-track averaged data from TOPEX/Poseidon and Jason (http://volkov.oce.orst.edu/tides). The tidal simulation quality is improved by assimilating longer satellite time series (on TOPEX/POSEIDON tracks since 2002) with more tidal gauge stations (Egbert et al., 1994; Egbert and Erofeeva, 2002). The river discharges at Datong hydrological station were obtained from widely used, archived daily measurements provided by Changjiang Water Resources Committee (http://www.cjw.gov.cn/).

Remote sensing detection provided spatial information of land-use types uncovered by water. The tidal creeks wider than 5 m were interpreted from Landsat8 OLI/TIRS C1 Level-1 product obtained on 20 September 2020. The lower boundary of the tidal flat was extracted from the Sentinel-2 product during a low spring tide (03 October 2019). The higher boundary of the wetland was defined at the toe of the seawall, interpreted from the Landsat8 images during high spring water (15 August 2020). All

the satellite images were downloaded from USGS archived database (http://glovis.usgs.gov/), with resolutions varying from 10 m to 30 m. The accuracy of water boundary interpretation was estimated to be higher than 0.2 m (Kang et al., 2017). The saltmarsh species were interpreted from Landsat8 images obtained on 19 November 2014, with a distinct zonal pattern of *P.australis*, *S.mariqueter*, and bare tidal flat distributed from near dike to the seaside. The vegetation transitional boundary was determined by the dominant species with field surveys during August 2015. The statistical saltmarsh metrics of density, stem height, and canopy diameter used for explicit vegetation modelling were obtained by RIEGL 3D laser scanner (Fig. 1b-g, detailed parameters are referred to Chong et al., 2021).

3.2. Numerical model setup

The large-scale model was constructed based on coupling TELEMAC-2D model and TOMAWAC model. TELEMAC-2D solves the Saint-Venant equations using the finite-element differential computation, while TOMAWAC solves wave propagation using the direction decoupling formula and the full-wave spectrum formula (http://www.opentelemac.org/). Both modules were internally coupled, resolving irregular triangular meshes considering wave-current interactions and wave set-ups. This means the TOMAWAC module passed the information on radiation stresses to the TELEMAC-2D module, and the TELEMAC-2D module returned information on the free surface and flow velocity to the TOMAWAC module (Zhang et al., 2018). The coupled models used the same set of irregular triangular meshes (Fig. 3a), denser at nearshore and courser at offshore, resulting in 45% of the total meshes (34,869) in the Yangtze Estuary. The landward boundary was extended 600 km upstream to the Datong hydrological station, the tidal limit of Yangtze Estuary (Zhang et al., 2016), imposed with measured daily river discharges. The ocean boundary was imposed with the TPXO tide model. The 40-years long time series, 10 m-height wind velocities downloaded from ECMWF were imposed on ocean surfaces of every triangular node. The large-scale wind field ensured the full development of wind waves and swells, which were passed to drive the local-scale model after statistical processing (Fig. 2). All the boundary data were vectors in time. Therefore, the finite element differential calculation was computed synchronously over time
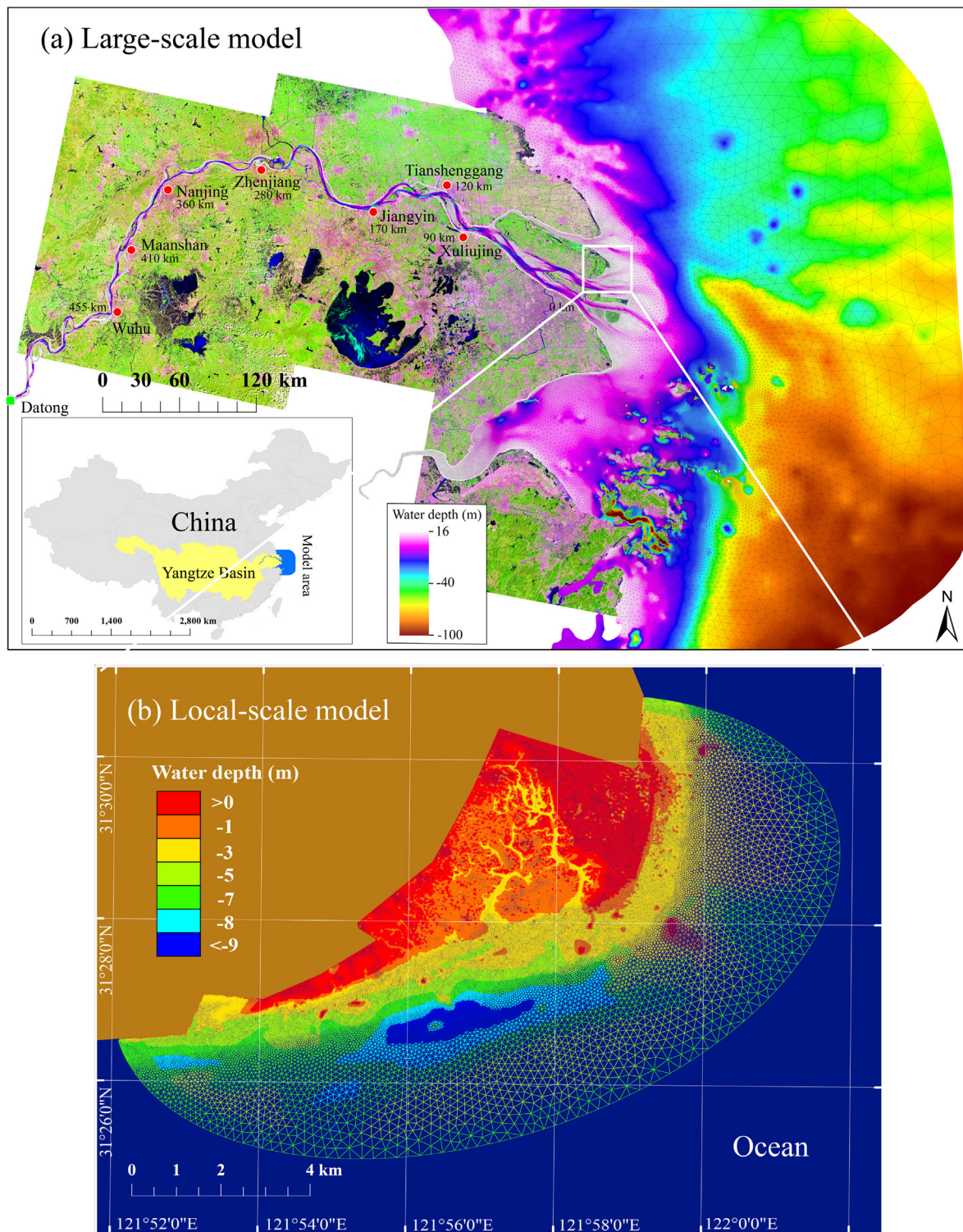
Fig. 3. The display of water depth and triangular meshes for (a) the Yangtze Estuary large-scale model and (b) the Chongming Dongtan Shoal (CDS) local-scale model. The ocean boundary of the nested local-scale model was statistically derived from the analysis of the large-scale model output.

and space in the mesh grid. The detailed configurations of the large-scale model and the calibration/validation using the field measurements obtained from anchored boat observations were referred to Zhang et al. (2018, 2021).

The output of the large-scale model consists of 40 years long, hourly tides and waves from 1979 to 2020 (Zhang et al., 2021). Based on this, the monthly maximum tides and waves close to CDS were extracted (Zhang et al., 2021), representing extreme weather conditions, e.g., a possible superposition of strong wind, storm surge, and high spring tide. We used

the exceeding probability of cumulative distribution function (CDF) to express the recurrence level of each hydrodynamic parameter, whose reciprocal is defined as the return period T, representing an event occurring in any year with the probability of $1/T$ (Cheng et al., 2014). The designed return levels of those hydrodynamic parameters (Table 1), based on the selection of suitable probability density functions (PDF) (Appendix Fig. A1), were used to drive the ocean boundary of the local-scale model (Fig. 3b) for scenario simulations. The purpose of using statistical return levels to drive the

Table 1

The design of hydrodynamic boundary condition imposed on Chongming Dongtan Shoal (CDS) model.

Return Period(P/yr)	Surge (m)	Tide (m)	SWHs (m)	Peak wave period (s)	wave direction (°)
1/100	1.39 (1.11–1.73)	2.08 (2.07–2.09)	2.50 (2.20–2.96)	6.63 (6.16–7.19)	160
1/200	1.45 (1.16–1.81)	2.09 (2.08–2.10)	2.76 (2.35–3.30)	6.92 (6.37–7.61)	160
1/500	1.54 (1.23–1.91)	2.10 (2.09–2.11)	3.05 (2.53–3.76)	7.29 (6.62–8.15)	160
1/1000	1.60 (1.29–1.99)	2.10 (2.09–2.12)	3.26 (2.66–4.13)	7.55 (6.79–8.55)	160
1/2000	1.66 (1.34–2.06)	2.11 (2.10–2.12)	3.48 (2.78–4.30)	7.80 (6.95–8.75)	160
1/5000	1.74 (1.41–2.15)	2.11 (2.10–2.13)	3.77 (2.94–4.30)	8.00 (7.13–8.75)	160

boundary was to capture the magnitude of long-term trends indicative of possible future climate changes. The uncertainty of the boundary parameters will pass to the variance of wave modelling results. Here, the uncertainty of 95% confidence level, considering the criteria of breaking wave height to the water depth ratio, for all parameters involved at the boundary is presented in Table 1.

To downscale the large Yangtze Estuary model to a more accurate near-shore wave propagation, the local-scale model of TOMAWAC covering CDS was constructed (Fig. 3b). Consistent with TELEMAC-2D, TOMAWAC was based on the same set of the triangular mesh. In this case, the grid resolution varies from 10 m near the dike to 200 m offshore, with a refined grid resolution of 5 m in the tidal creeks. The resulting finite volume grid contains 75,500 nodes, of which approximately 70% of the elements are located in the wetland area. The land boundary of the CDS model was set 10 m behind the dike to absorb the tide and wave energy. Storm surges and waves were set on the offshore boundary, approximately ~4 km away from the bare tidal flat. The offshore boundary forces of tides, surges, and SWHs were the designed return levels statistically derived from the large-scale model output (Table 1).

The wave propagation, attenuation, and conversion processes by the interactions with saltmarsh morphology and saltmarsh vegetation were simulated with a customized spatial propagation scheme. These were implemented in TOMAWAC using the BJEB formula (Battjes and Janssen, 1978; Eldeberky and Battjes, 1995) for depth-induced wave breaking, revised Madsen bottom friction formula (Madsen et al., 1988; Baron-Hyppolite et al., 2019) for effectively implementing the Manning "M" as an adjusted friction length, and JONSWAP for spectral wave model at the boundary with standard shape parameters of $\gamma = 3.3$, $\sigma_a = 0.07$, and $\sigma_b = 0.09$ (Zhang et al., 2021). Notably, depth-induced wave breaking is essential for this research occurs when waves propagate into shallow water, and the wave height can no longer be supported by the water depth. The formulation of wave breaking is based on the breaking model of Battjes and Janssen (1978) revised by Eldeberky and Battjes (1995), where the spectral shape is not influenced by breaking. The source term due to depth-induced wave breaking is written:

$$S_{dep}(\sigma,\theta) = -\frac{\alpha Q_b \overline{\sigma} H_m^2}{8\pi} \frac{E(\sigma,\theta)}{E_{tot}} \qquad (1)$$

where, α is a calibration constant, Q_b is the fraction of breaking waves, $\overline{\sigma}$ is the mean relative frequency, E_{tot} is the total wave energy, $H_m = \gamma d$ is the maximum wave height, and Gamma γ is the free breaking parameter (a wave height - to depth ratio). Based on laboratory and field data, it has been shown that the breaking Gamma parameter γ varies depending on the wave conditions and the bathymetry. Here, we used the Ruessink et al. (2003) empirical formulation to calculate the Gamma parameter, which is determined as a function of the local wave number k and the water depth d,

$$\gamma = 0.76kh + 0.29. \qquad (2)$$

3.3. Coastal restoration scenarios

NBFD scenarios such as engineering works and artificial interventions were compared with natural saltmarsh on wave attenuation. Six scenario simulations were designed to investigate the vegetation, morphology, and engineering effects, i.e., the removal or including of saltmarsh morphology and saltmarsh vegetation, building submerged breakwaters, application of standard timber piles and sand nourishment (Fig. 4). The field measured bathymetry and interpreted vegetation during the summer of 2020 were regarded as the natural saltmarsh of CDS, where the intertidal sedimentary layer was assumed to be created by saltmarsh accretion. In contrast, the initial coastal mudflat before accretion refers to the saltmarsh sedimentation layer removal. The description of the six designed NBFD scenarios are:

(I) The scenario of saltmarsh morphology (marsh,noveg). This scenario was the natural CDS wetland with vegetation removal, representing the bare tidal flat formed by natural saltmarsh accretion (Fig. 4b). This was designed to calculate the contribution of the saltmarsh morphology (the vegetational sedimentary layer) on wave attenuation.

(II) The scenario of initial coastal mudflat (flat,noveg). This scenario represented the original intertidal space between mean high-water spring (MHWS) and mean low-water spring (MLWS) before the saltmarsh morphology was formed, indicating the initial coastal mudflat morphology without vegetation accretion (Fig. 4a). In this condition, the mudflat landform was produced by extracting bottom elevation in the tidal creeks and interpolated to generate a consistent resolution of DEM as saltmarsh morphology$_{(marsh,noveg)}$, since creeks bottom elevation was approximately equal to the tidal flat height at the marsh edge.

(III) The scenario of saltmarsh morphology with summer vegetation attached (marsh,veg). This scenario represented the natural condition of the summer CDS wetland surveyed during August 2015, containing *P.australis*, *S.mariqueter*, and bare tidal flat distributed from near dike to the seaside (Appendix Fig. A2), considering both the saltmarsh morphology and summer vegetation (Fig. 4c). Detailed saltmarsh species and vegetation settings were described in Section 3.4.

In addition to the natural saltmarsh-based accretion and wave attenuation, artificial engineering measures were tested for coastal restorations. The designed scenarios were:

(IV) The scenario of timber piles (flat,tp). A designed density of timber piles (0.3 m standard diameter, QMWS, 2019) through testing were placed in the intertidal space of the initial coastal mudflat$_{(flat,noveg)}$ to mimic the stiff stem structure such as mangroves for wave attenuation (Fig. 4d).

(V) The scenario of submerged breakwater (flat,sb). A designed height of submerged breakwater through testing was placed nearshore of the initial coastal mudflat$_{(flat,noveg)}$ to simulate wave attenuations by engineering works, simultaneously allowing sediment-rich water to pass through with proper openings even during normal tides (Fig. 4e).

(VI) The scenario of sand nourishment (flat,sn). An artificial sand supplement was designed to offset the possible future sediment flux shortage. The thickness of sand layer through testing was placed on top of the saltmarsh morphology$_{(marsh,noveg)}$ to calculate the wave attenuation by the artificial morphology layer (Fig. 4f).

The artificial engineering works such as the submerged breakwater$_{(flat,sb)}$ and timber piles$_{(flat,tp)}$ not only had a direct wave attenuation capacity but also would trap suspended sediment, hence providing an additional effect of wave attenuation through accretion. With proper coastal management,
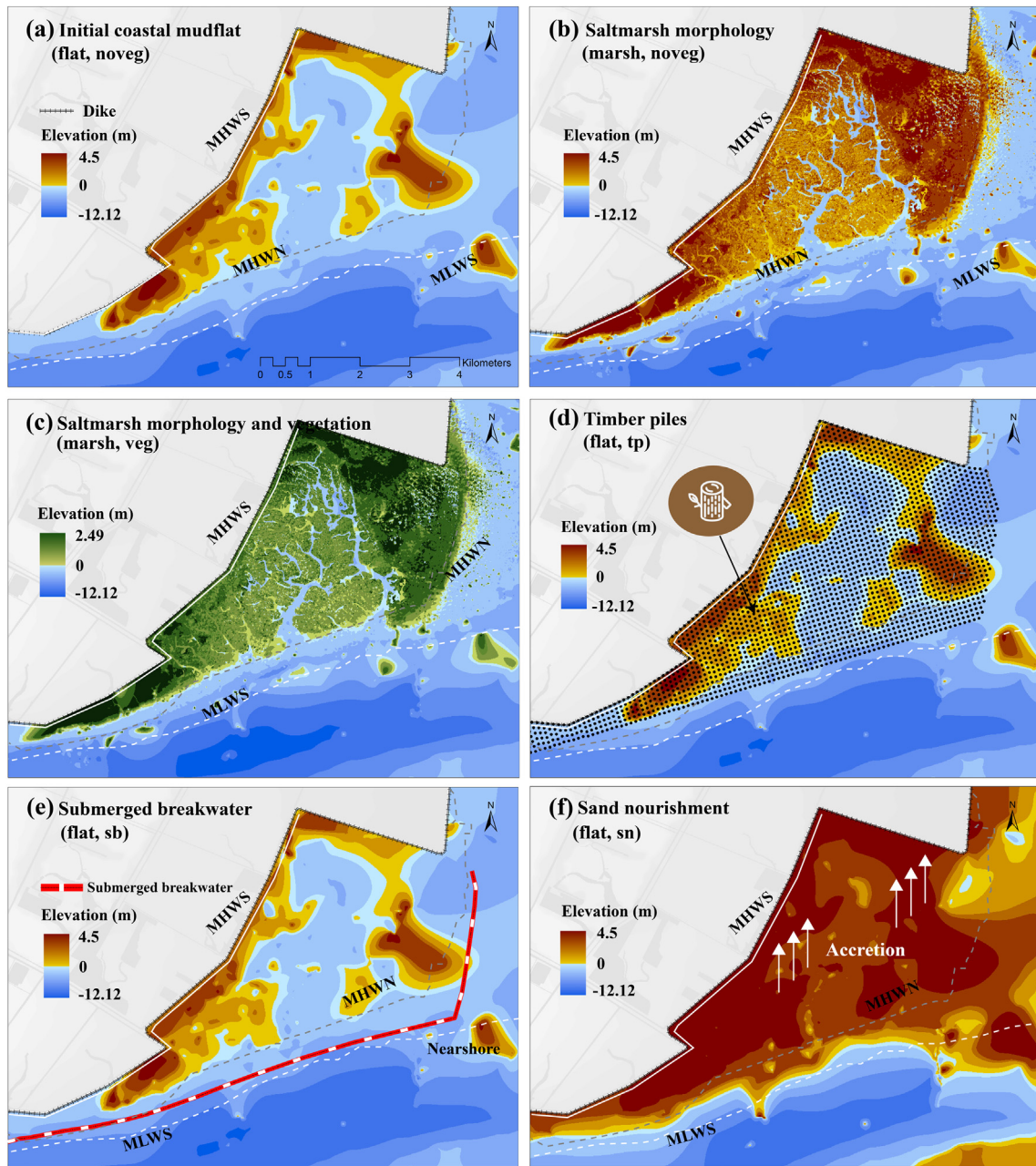
Fig. 4. Bathymetries and the scenario designs of the Nature-Based Flood Defense (NBFD) measure. (a) The scenario of initial coastal mudflat$_{(flat,noveg)}$, (b) The saltmarsh morphology$_{(marsh,noveg)}$, (c) The scenario of saltmarsh morphology with attached vegetation$_{(marsh,veg)}$, (d) The scenario of timber piles$_{(flat,tp)}$, (e) The scenario of submerged breakwater$_{(flat,sb)}$, (f) The scenario of sand nourishment$_{(flat,sn)}$.

the thickness of the artificial morphology layer equivalent to summer vegetational wave attenuation$_{(marsh,veg)}$ of CDS could be estimated.

3.4. Vegetation modelling approaches

The modelling of coastal saltmarsh on wave attenuation mainly includes three processes, i.e., depth-induced wave breaking, bottom friction by the morphology, and vegetational wave attenuation. Firstly, depth-induced wave breaking was the process of wave energy dissipation when the water was too shallow to support the high waves, i.e., reach a limiting wave height/depth-ratio (Baron-Hyppolite et al., 2019). For this case, the work done in the spectral wave module is based on the formulation of Battjes and Janssen (1978) with the specified Gamma parameter following Ruessink et al., 2003 as shown above. Secondly, as wave propagated onto

the tidal flat, the orbital wave velocity penetrated the shallow water, and the source function due to wave-bottom interaction became essential (Baron-Hyppolite et al., 2019). The effect of bottom friction on wave dissipation was represented by means of the Madsen formula (Madsen et al., 1988). In the TOMAWAC modelling, the magnitude of the Nikuradse friction length (k_N) was converted from an a-priori Manning roughness coefficient (n) provided by the United States National Land Cover Data base (U.S. Geological Survey, 2016) using the formula of Baron-Hyppolite et al. (2019). Thirdly, the wave attenuation by the 3D vegetation structure of stems and leaves were defined as the vegetation bulk drag force C_D, which was often considered to vary with the Reynolds number Re (Méndez et al., 1999; Pinsky et al., 2013) or the Keulegan-Carpenter number KC (Méndez and Losada, 2004) based on the work of Dalrymple et al. (1984).

Here, two vegetation modelling approaches on wave attenuation were developed, i.e., the implicit vegetation modelling by setting the 2D-enhanced bottom friction and the explicit vegetation modelling by setting the 3D-bulk drag force on an immersed body. For the implicit vegetation modelling, the process of vegetation-induced wave attenuation was treated the same as bottom frictions, made to represent the increased resistance that occurs when the waves interact with the saltmarsh; hence vegetation-induced wave attenuation and bottom frictional dissipation were combined into a uniform enhanced Nikuradse friction coefficient, which was mostly obtained by calibration (Vuik et al.,2016). For this case, Nikuradse roughnesses of *P.australis*, *S.mariqueter*, and bare tidal flat were set to $k_N = 0.12$ m (Manning friction M = 13 m$^{1/3}$/s, $n = 0.07$ s/m$^{1/3}$), $k_N = 0.014$ m (M = 28 m$^{1/3}$/s, $n = 0.035$ s/m$^{1/3}$), and $k_N = 0.002$ m (M = 40 m$^{1/3}$/s, $n = 0.025$ s/m$^{1/3}$), respectively, according to calibration and validations (Zhang et al., 2018; Zhong et al., 2021). The bottom friction for the deep ocean and the tidal channels were set to $k_N = 0.001$ m (M = 45 m$^{1/3}$/s, $n = 0.022$ s/m$^{1/3}$). In contrast, the explicit vegetation modelling further separated the function of vegetational bulk drag force from the bottom friction by considering the 3D-physical turbulence of vegetation on wave mitigation. In this case, the bottom friction of tidal flat was set to $k_N = 0.02$ m (M = 26 m$^{1/3}$/s, $n = 0.038$ s/m$^{1/3}$), while vegetation was represented as a field of stiff cylinders, allowing them to assign vegetation characteristics to the cylinders. The wave attenuation by stiff cylinders of the plant was calculated with the source term approach, which takes the effects of the vegetation into account by introducing a decay term to reduce the wave energy behind it (Perthame and Simeoni, 2001; Mentaschi et al., 2018). Assuming a uniform distribution of leaves over the plant, the contribution from the source term (S_{st}) due to the effect of a plant and the convective transport (S_{ct}) to the time-deriative wave action density could be written as:

$$S_{st}(\sigma, \theta) = -\frac{c}{A} c_g E(\sigma, \theta),$$ (3)

$$S_{ct}(\sigma, \theta) = -\frac{1}{A} \sum (F_n \cdot \Delta l),$$ (4)

where A is the area of the cell in the mesh in which the plant is located, c is the reflection factor, c_g is the group celerity, $E(\sigma, \theta)$ is the energy density, F_n is the normal flux through the element edge, Δl is the length. The proposed approach differs from the classical drag force approach of Dalrymple et al. (1984) and Méndez et al. (1999; 2004), is based on spatial propagation schemes because it provides a local representation of cylinders for the parameterization of energy dissipation due to unresolved obstacles in spectral wave model. This approach consists in correcting energy fluxes estimated by the spatial propagation scheme based on transparency coefficients of obstructed cells, allowing not to reformulate, reimplement, and revalidate the parameterization of cylinders for each propagation scheme (Mentaschi et al., 2018; Chen et al., 2021; Gijón Mancheño et al., 2021).

3.5. Cost-benefit analysis

The benefit of a flood protection measure, often represented by the Net Present Value (NPV), is defined as the present value converted from the future reduced losses subtracting the costs, indicating the net benefit after implementation of the measure. Here, the cost of the designed engineering and non-engineering measures were evaluated using Net Present Value (NPV) and Cost-Benefit Ratio (BCR). Meanwhile, the reduced losses were defined as the reduced construction and maintenance costs of hard seawall, e.g., the reduced investment cost of the wave barrier previously installed on top of the seawall (Table 2), to achieve an equivalent flood protecting standard (Zhang et al., 2021). The criteria of optimization BCR was determined by calculating the NPV for different measures achieving the same wave attenuation effect.

$$NPV = \sum_{t=0}^{T} \frac{B_t - C_t}{(1+r)^t},$$ (5)

$$BCR = \sum_{t=0}^{T} \frac{B_t}{(1+r)^t} / \sum_{t=0}^{T} \frac{C_t}{(1+r)^t},$$ (6)

where B_t is the benefit and C_t is the cost after t years investment, including the initial investment and annual maintenance costs, which are shown in Table 2. Three different discount rates, r, were considered here, i.e., China's current official discount rate 8% as the upper limit, the long-term benefit encouragement discount rate 4% as the lower limit, and a median rate of 6% is factored. T is the time, which was calculated according to the time required for natural deposition on CDS. If $BCR > 1$ and $NPV > 0$, the measure was considered economically attractive within the study period T. The most cost-effective measure leads to the minimum in both time-needed and investment-cost. Here, we only considered the benefit of flood mitigation, while other ecosystem service values were not accounted.

3.6. Model validation and comparison

Field observation was carried out at a selected cross-section on CDS (Fig. 1c) during spring tide from 15 June 2019 to 20 June 2019. Three sampling points placed at representative marsh zones from the dike toe to the low water boundary performed synchronous measurement (Fig. 5a), i.e., in the high marsh covered with *P.australis* (point A: 121°54′09″, 31°27′01″N), between middle marsh and high marsh partly covered with *P.australis* (point B: 121°54′12″E, 31°27′00″N), and in the bare tidal flat (point C: 121°54′14.00″E, 31°26′56″N). The straight-line distance between points A, B, and C were about 60 m and 120 m apart, respectively. Each gauge point was equipped with an RBR (Tide Wave Recorder-2050, TWR-2050) to measure the water and wave dynamics. The sensor probes fixed on tripods were placed about 10 cm away from the mud surface. The sampling frequency was set to 8 Hz with a working time of 512 s and collected every 20 min. This means 4096 data had been collected during measurement (Fig. 5a). The data during the high tide periods without local wind disturbance were used for validation (Fig. 5b,c).

The 2019 field measurement was carried out during the non-storm period, and we used published data during storm surges (Zhu et al., 2020) and an experimental flume measurement (Möller et al., 2014) for storm validations of the applied bottom frictions (Nikuradse roughnesses) in the

Table 2

The unit price of artificial wetland restoration measures according to the National Statistics Bureau of the People's Republic of China and NFGAP, 2018 (all units were converted to 2019 price based on the GDP deflator).

	1	2	3	4	5
	Artificial saltmarsh	Sand nourishment	Timber piles[a]	Submerged breakwater	Wave barrier
Unit price-construction	0– 2714.32US$	3US$	6.73US$	120.51US$	2376.64US$
Unit price-maintenance	0– 54.28US$	0.09US$	6.73US$	60.26US$	1188.20US$
Unit	ha	m³	per	m³	m³
Reference Year	2018	2020	2019	2019	2019
Source	NFGAP, 2018	Hinkel et al., 2013	QMWS, 2019	QMWS, 2019	QMWS, 2019

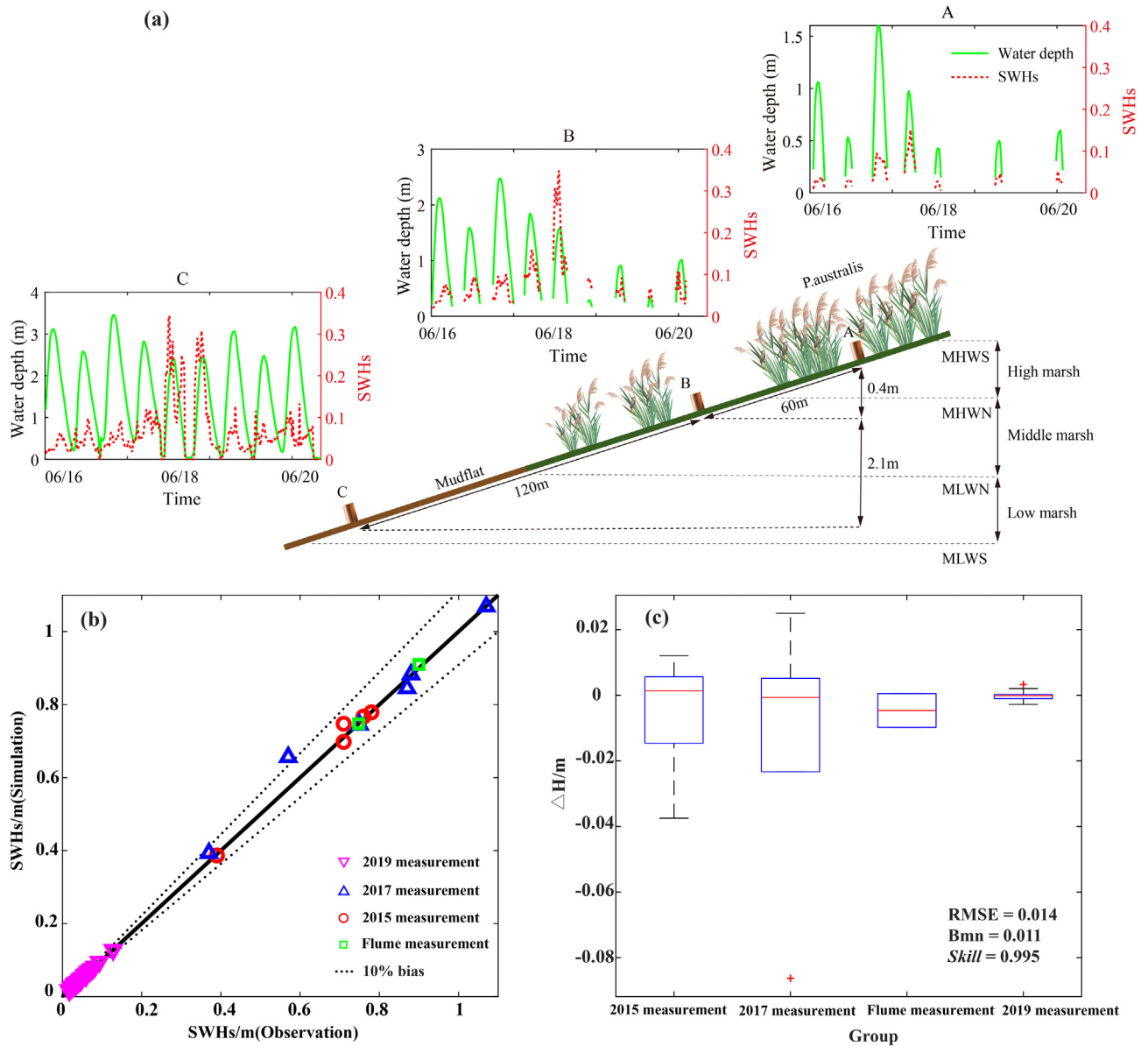[a] The diameter of the standard timber pile is 0.3 m (QMWS, 2019).

Fig. 5. Field measurement and model validation. (a) Sketch map showing the 2019 field measurement on Chongming Dongtan Shoal (CDS) and the measured hydrodynamic parameters of water depth and significant wave height. (b,c) The comparisons between modelling results and field measurements: purple triangles are the 2019 field measurement, blue triangles are the 2017 field measurement, red circles are the 2015 field measurement, and green squares are the flume experiment measurement.

implicit vegetation modelling. Validation was based on two sets of wave propagation measurements during storm periods, carried out by Zhu et al. on 11 January 2015 and 13 January 2017 at the Wadden Sea, using field measured bathymetry. Comparison with the indoor physical experiment of Möller et al. was based on wave propagation along a 40 m long flat bottom flume, configured with vegetations on the floor, 2 m depth water, and driven by 0.9 m-height, 4.1 s period waves. Finally, the simulation accuracy of SWHs for the three sources of validation was evaluated using root-mean-square error (RMSE), mean-normalized bias (B_{MN}) and *skill* value (Zhang et al., 2021). RMSE indicated the error magnitude, the smaller the value, the higher the accuracy; B_{MN} indicated the overestimation or underestimation of the simulation; *skill* value indicated the effectiveness of the simulation, the good validation was with $0.65 \le skill < 1$. Results showed that 98% of the comparisons were less than 10% error, and 90% were less than 5% error (Fig. 5b). The RMSE was 0.014 m, the B_{MN} was 0.011 m, and the *skill* value was 0.995, indicating good modelling validation of SWHs with the applied bottom frictions (Fig. 5c).

4. Results

4.1. The wave attenuation by designed NBFD measures

The wave propagation to the coastal area was attenuated by designed NBFD measures (Fig. 6). Figs. 6a,b,c directly reflected the combined and separated energy dissipation by the saltmarsh morphology and saltmarsh vegetation for the wave height attenuation, which showed a zonal pattern roughly following the intertidal elevation. The scenario of initial coastal mudflat$_{(flat,noveg)}$ (Fig. 6a) was not very effective in wave attenuation, which had only reduced by approximately 0.6 m (24% of the wave height given at the boundary, the reference of percentages are the same as follows), from the boundary of 2.5 m to 1.9 m at the toe of the seawall. The addition of saltmarsh morphology$_{(marsh,noveg)}$ (Fig. 6b) and saltmarsh vegetation$_{(marsh,veg)}$ (Fig. 6c) profoundly increased the wave height reduction to approximately 50% and 70%, respectively. Consequently, the natural sedimentary layer accreted by the saltmarsh of Chongming Dongtan Shoal
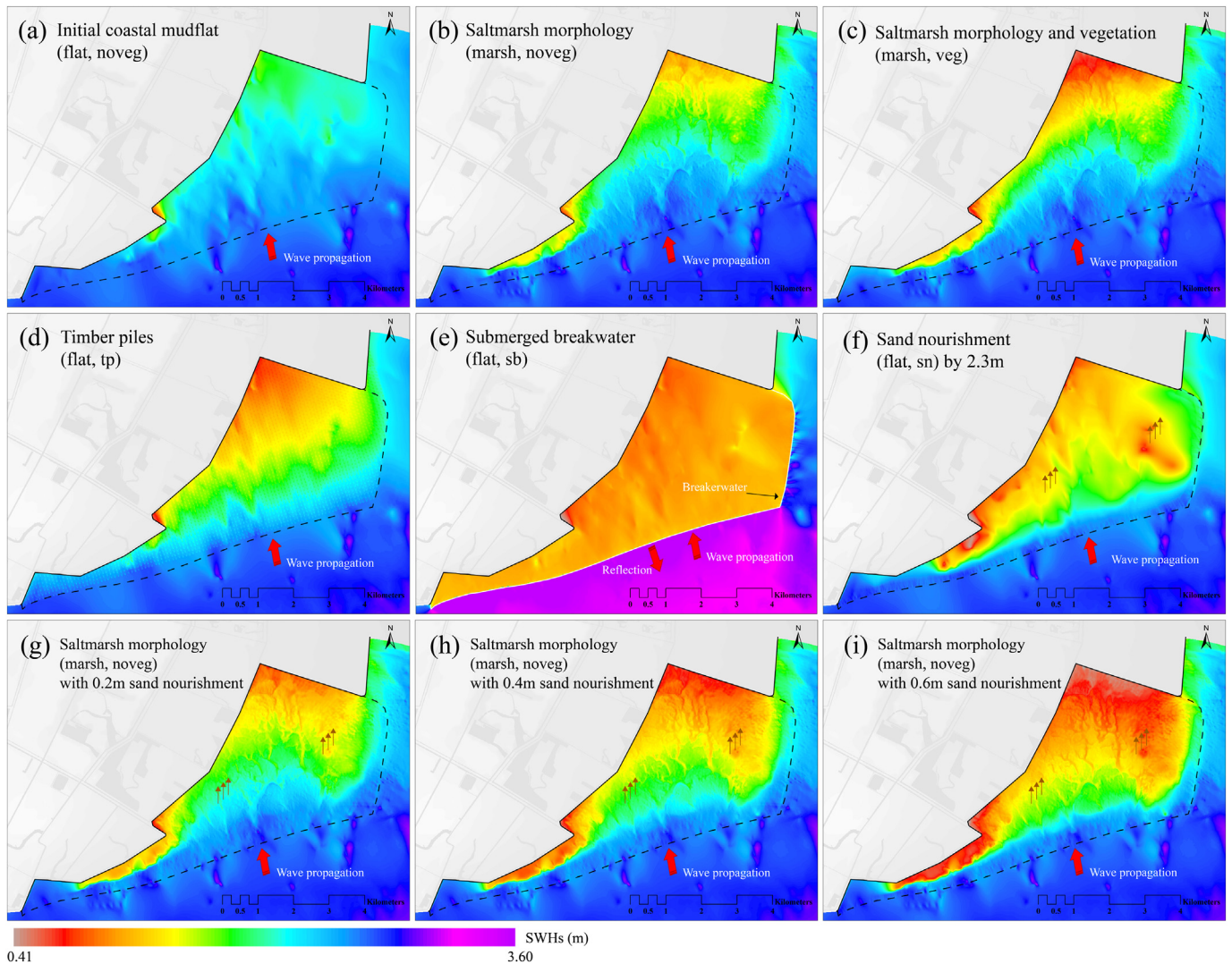
Fig. 6. Results of wave attenuations by Nature-Based Flood Defense (NBFD) under 500 yrs. return hydrodynamic boundary conditions for (a) the scenario of initial coastal mudflat$_{(flat,noveg)}$ (II), (b) the scenario of saltmarsh morphology$_{(marsh,noveg)}$ (I), (c) the scenario of saltmarsh morphology with attached vegetation$_{(marsh,veg)}$ (III), (d) the scenario of timber piles$_{(flat,tp)}$ (IV), (e) the scenario of submerged breakwater$_{(flat,sb)}$ (V), (f) the scenario of sand nourishment$_{(flat,sn)}$ (VI) by 2.3 m, (g,h,i) are the scenario of saltmarsh morphology$_{(marsh,noveg)}$ with 0.2 m, 0.4 m, and 0.6 m sand nourishment, respectively.

(CDS) contributed approximately 30% to the wave attenuation, and the attached saltmarsh vegetation further contributed approximately 20% to the wave attenuation. Including the effect of initial coastal mudflat$_{(flat,noveg)}$, the combined effect of CDS wetland could attenuate the wave heights by approximately 74% in summer conditions under impacts of 500 yrs. return level storms (Fig. 6c). Under other storm scenarios (100 yrs. ~ 5000 yrs), wave attenuation percentages for scenarios SWH$_{(flat,noveg)}$, SWH$_{(marsh,noveg)}$, and SWH$_{(marsh,veg)}$ are referred to in Table 3.

With artificial interventions, to achieve a similar wave attenuation as the natural saltmarsh$_{(marsh,veg)}$ of CDS (Fig. 6c), engineering solutions

Table 3
The wave attenuation percentage by initial coastal mudflat, saltmarsh morphology, and saltmarsh vegetation under return storm levels of 100 yrs. ~ 5000 yrs.

Wave reduce percentage Storm scenarios	SWH$_{(flat,noveg)}$	SWH$_{(marsh,noveg)}$	SWH$_{(marsh,veg)}$
100 yrs	20% (18%–24%)	49% (48%–53%)	73% (72%–74%)
200 yrs	21% (20%–24%)	52% (50%–54%)	74% (74%–75%)
500 yrs	24% (22%–26%)	54% (51%–56%)	74% (74%–75%)
1000 yrs	27% (25%–30%)	56% (52%–57%)	74% (74%–76%)
2000 yrs	31% (29%–34%)	58% (55%–61%)	75% (74%–77%)
5000 yrs	35% (32%–37%)	61% (59%–65%)	76% (75%–77%)

such as timber piles$_{(flat,tp)}$, submerged breakwater$_{(flat,sb)}$, and sand nourishment$_{(flat,sn)}$ were examined (Fig. 6d,e,f). For the scenario of sand nourishment$_{(flat,sn)}$, the artificial sedimentary layer thickness should be increased by 2.3 m on top of the initial coastal mudflat$_{(flat,noveg)}$ (Fig. 6f), which was roughly equivalent to adding 0.4 m of the sedimentary layer to the present CDS bare tidal flat$_{(marsh,noveg)}$ (Fig. 6h). For the scenario of timber piles$_{(flat,tp)}$, 0.3 m diameter of standard timber piles should be set to 4 piles/10m² on the initial coastal mudflat$_{(flat,noveg)}$ (Fig. 6d). For the scenario of the submerged breakwater$_{(flat,sb)}$, the initial coastal mudflat$_{(flat,noveg)}$ should be constructed with a 0.7 m crest level (relative to mean-sea level) of the submerged breakwater at the low water boundary, which rapidly reduced the wave height by approximately 53% behind the breakwater (Fig. 6e). However, the further change of wave height on the tidal flat was very gentle with no obvious wave-breaking zone. The function of the submerged breakwater was to break waves like the marsh edge cliffs, which reflect and reduce waves, forming an intensive wave-conflicting zone at the front edge of the tidal flat when superimposing with the incoming waves (Fig. 6e).

In addition to wave attenuation, saltmarsh and engineering works were effective in trapping sediments. This was an important value of NBFD measures in the long run, which helped mitigate waves by raising the marsh platform elevation. It was estimated that an additional 0.4 m sedimentation

layer increase on top of the current tidal flat$_{(marsh,noveg)}$ (Fig. 6h) was similar to wave attenuation by the summer saltmarsh$_{(marsh,veg)}$ of CDS. Thus, the wave attenuation capacity of the vegetation structure of summer saltmarsh on CDS was equivalent to a sand nourishment thickness of 0.4 m. Sensitivity tests indicated that a lower sedimentary layer increase (e.g., 0.2 m, Fig. 6g) or a larger sedimentary layer increase (e.g., 0.6 m, Fig. 6i) would underestimate or overestimate wave attenuations by 8% and 7%, respectively. The wave attenuations under other storm surge and wave conditions, e.g., 50 yrs. ~ 5000 yrs. return levels, were referred to in Appendix Fig. A3.

4.2. Contribution of saltmarsh morphology versus saltmarsh vegetation to wave attenuation

The nearshore storm wave propagation was dissipated by both saltmarsh vegetation and saltmarsh morphology, which were two of the main contributors to marshy wave energy dissipation (Fig. 7). We observed that local wave dissipation rate varied with the topography (e.g., the influence of tidal creeks), while at a large scale, the wave dissipation rate increased along with propagation, showing a zonal spatial distribution following intertidal elevation. If the saltmarsh morphology was removed, the wave attenuation by saltmarsh vegetation of CDS (i.e., initial coastal mudflat$_{(flat,noveg)}$ configured with *P.australis* and *S.mariqueter*, Fig. 7b,e,h) was significantly smaller than those of the saltmarsh morphology$_{(marsh,noveg)}$ condition (Fig. 7a,d,g). Even single high vegetation (*P.australis*) was configured, the wave dissipation capacity became greater (Fig. 7c,f,i), but was still

smaller than that of the morphology$_{(marsh,noveg)}$ condition (Fig. 7a,d,g). Under varying storm conditions examined (e.g., 50 yrs. ~ 5000 yrs. return levels), we calculated a larger contribution of wave dissipation (65–78%) from the saltmarsh morphology and a minor contribution (22–35%) from the saltmarsh vegetation (Fig. 8). The relative contribution of the saltmarsh morphology compared to the saltmarsh vegetation on wave attenuation showed a continuous increase with the increase of storm grades. Compared with the above-ground vegetation structure, which was fragile during storm impact, the consolidated sedimentary layer of the saltmarsh morphology was more stable (Leonardi et al., 2018) and provided more efficient wave attenuations even under extreme storm surge conditions. Thereby, we concluded that if the function of saltmarsh morphology was considered part of the NBFD solution, the uncertainty of saltmarsh-based coastal protection can be reduced in practice.

To examine the impacts of saltmarsh morphology and saltmarsh vegetation on wave attenuation in detail, the chainage wave variation along the white profile in Fig. 8 is shown (Fig. 9). Overall, the wave dissipation percentage contributed by the saltmarsh morphology was overwhelmingly dominant over saltmarsh vegetation after the middle intertidal elevation and showed a continuous increase with propagation. The wave attenuation by the saltmarsh morphology$_{(marsh,noveg)}$ condition was almost linearly correlated with the intertidal width (Fig. 9 red line), but the vegetational wave attenuation intensity was sensitive to the attached saltmarsh species. For a single vegetation (*P.australis*) scenario, a quick wave energy dissipation occurred at the front edge of tidal flat (0-1000 m), and a gentle wave dissipation further inshore at the high intertidal zone. For the mixed vegetation
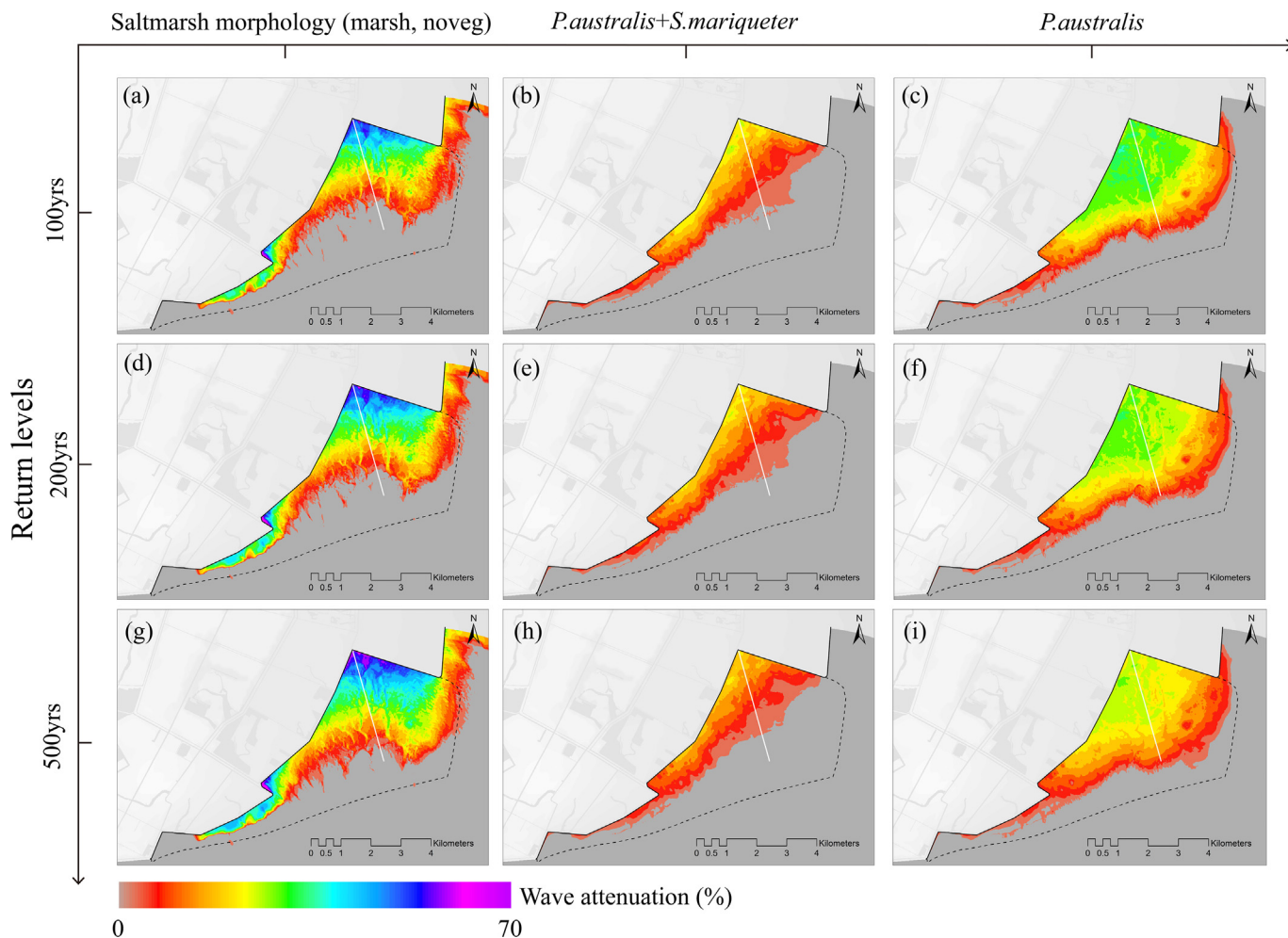

Fig. 7. Accumulated wave attention percentage from tidal front to the toe of seawall under the scenario of storm return levels 100 yrs., 200 yrs., and 500 yrs. contributed from (a,d,g) saltmarsh morphology$_{(marsh,noveg)}$, (b,e,h) the mixed vegetations scenario of *P.australis* and *S.mariqueter*, and (c,f,i) the single vegetation scenario of *P.australis*.
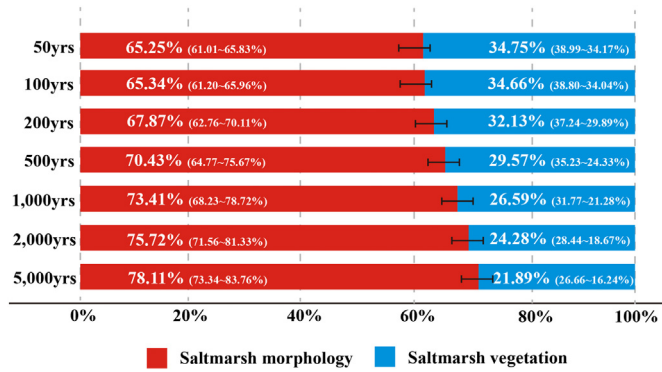
Fig. 8. Comparison of the relative contribution to wave attenuation between saltmarsh morphology and saltmarsh vegetation under varying storm conditions.

(a more realistic scenario with pioneer species *S.mariqueter* in front of the high marsh species *P.australis*) scenario, the wave energy dissipation by the pioneer plant of *S.mariqueter* at the low intertidal zone was less intensive, which lowered the overall wave energy dissipation rate and produced a uniform distribution along with the distance. Notably, the wave energy dissipations by the mixed vegetation configuration varied linearly (green line in Fig. 9), indicating a pattern of uniform energy dissipation (van der Wegen et al., 2008); while the wave energy dissipations by the single vegetation configuration varied exponentially (blue line in Fig. 9), indicating a pattern of uniform entropy production (Leopold and Langbein, 1962).

4.3. Comparison of wave attenuations by implicit and explicit vegetation modelling

Numerical inquiring of wave attenuation with configurations mimicking the summer vegetation condition of CDS (including *P.australis* and *S. mariqueter*) was examined under 500 yrs. storm return levels. The overall spatial pattern of wave attenuation by the explicit vegetation modelling was similar to the calibrated implicit vegetation modelling (Fig. 10a,b), with dissipated wave height by approximately ~76% from the implicit vegetation modelling compared with approximately ~84% from the explicit vegetation modelling. Specifically, the wave attenuation by the implicit vegetation modelling was more intensive on the high intertidal zone. In contrast, the explicit vegetation modelling dissipated more wave energy on the low intertidal zone. The difference in the spatial pattern is due to the inconsistency of the wave dissipation mechanism, i.e., the implicit vegetation modelling dissipates wave energy through the bottom sensitivity of the penetrated waves, dependent on the near-bottom orbital velocity. In contrast, the explicit vegetation modelling dissipated a tremendous amount of wave energy at the vegetation front edge through intensive wave-cylinder interactions (Fig. 10b). Overall, the total energy dissipation as a system was similar by the two approaches, with a local difference of wave height attenuation at around ±0.2 m (Fig. 10d).

The implicit vegetation modelling differentiated land-use types based on standard tables with calibrated Manning values. In addition to depth-induced wave breaking, the Nikuradse roughnesses calibrated in this study represented the collective frictions of saltmarsh morphology and saltmarsh vegetation. By contrast, the explicit vegetation modelling dissipated wave energy with the disturbance effect of each plant; therefore,
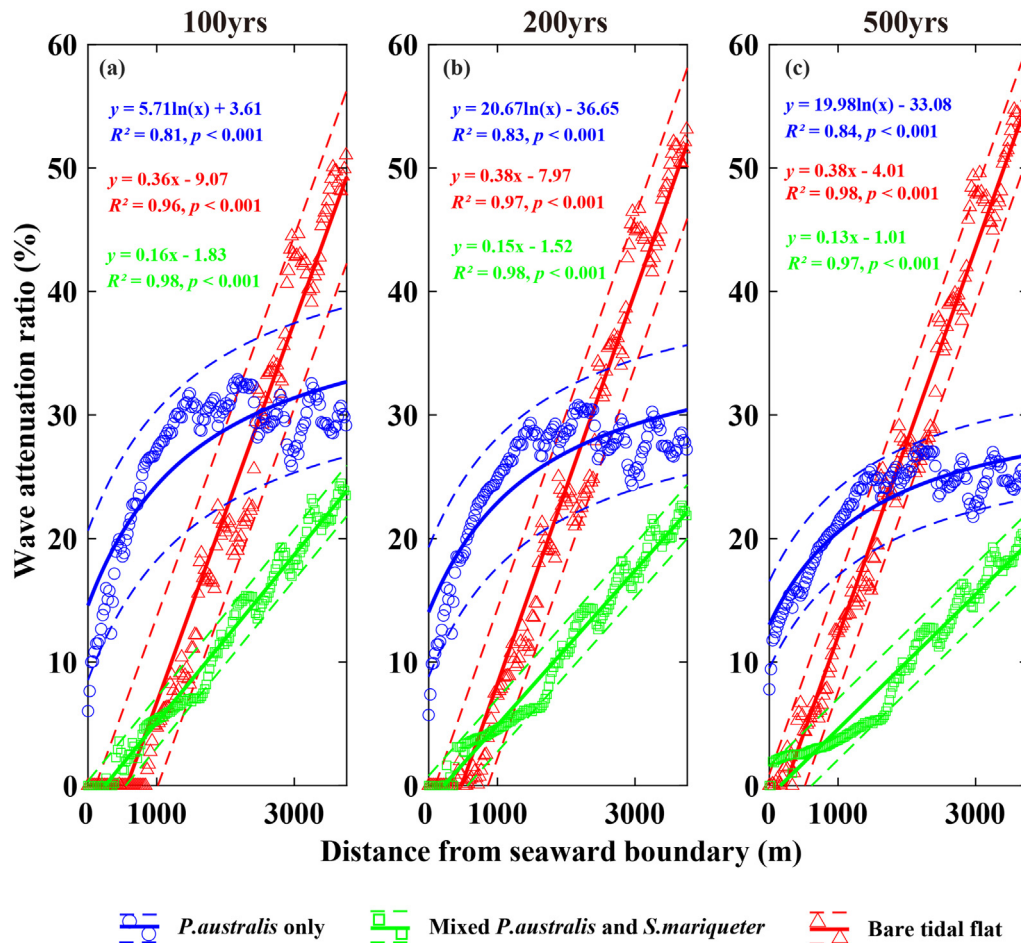

Fig. 9. Comparison of chainage wave attenuation rate along a representative section in Fig. 7. The red, blue, and yellow fitted models show wave attenuation by saltmarsh morphology, single vegetation scenario of *P.australis*, and mixed vegetation scenario of *P.australis* and *S.mariqueter*, respectively. Dash lines are the 95% confidence interval.
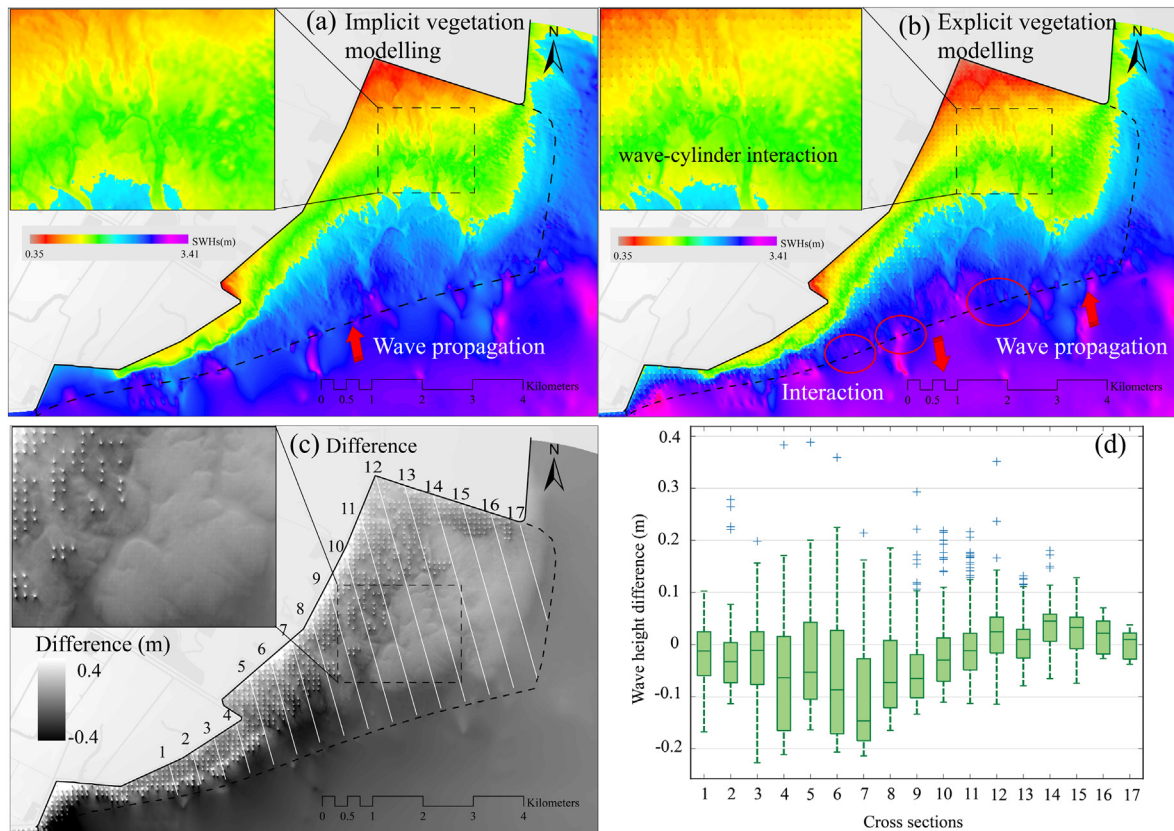
Fig. 10. Comparison of wave dissipations under two vegetation modelling approaches: (a) implicit vegetation modelling approach, (b) explicit vegetation modelling approach, (c) the wave height difference between (a) and (b), (d) the wave height difference on representative profiles of (c), with the upper and lower box edges representing the 25% and 75% quartiles, and the blue points indicates outliers.

the advantage was to display the wave dissipation of vegetation monomer in detail. The difference in wave dissipation mechanism between the two approaches was displayed with the spot texture pattern obtained from subtracting the explicit vegetation modelling result to the implicit vegetation modelling result (Fig. 10c). However, the explicit vegetation modelling for wave disturbance was based on the source term and convective flux calculation, which was more computationally costly than the conventional Madsen bottom friction calculation. For example, to model the wave attenuation on CDS (~42km²) under 500 yrs. storm condition, it took over 17 h for the explicit vegetation modelling compared with only 6 h for the implicit vegetation modelling. Moreover, the explicit vegetation modelling generated strong wave-cylinder interactions at the front edge of the tidal flat (pink stripes in Fig. 10b), especially where the cylinder density was high. The outliers of the wave height difference shown in Fig. 10d were due to the increased wave-cylinder interaction by stiff stem and canopy. Consequently, the cylinder approach seems more suitable for modelling woody plants such as mangroves and shrubs (Chen et al., 2021; Gijón Mancheño et al., 2021) but was not fit for modelling flexible herbaceous.

4.4. Cost-benefit analysis

To provide a broader reference, the costs and benefits of the three nature-based engineering works were investigated (Fig. 11; Appendix Table A1). Under extreme storm impacts, the wave attenuation by setting standard timber piles(flat,tp) with a density of 4 per 10m² on the initial coastal mudflat(flat,noveg) was measured equivalent to the construction of a submerged breakwater(flat,sb) at the low water boundary with a height of 0.7 m crest elevation, which was further equivalent to a 0.4 m thickening of saltmarsh morphology layer(flat,sn) (or a 2.3 m sand nourishment on top of the initial coastal mudflat(flat,noveg)). All three measures were designed to reduce the same wave height by approximately 70%, which allowed a direct

comparison of their cost-effectiveness. According to the field measurement of vertical accretion rate (0.06 m/yr) on CDS (Li et al., 2014), it would take approximately 38 years to accrete 2.3 m. Considering the construction and maintenance costs over the 38 years, timber piles(flat,tp) would cost US$ 22 million (US$ 19–26 million, the numbers in brackets are the 95% confidence interval, same hereafter), while the submerged breakwater(flat,sb) would only cost US$ 8 million (US$ 7–9 million). In comparison, the natural saltmarsh measure was very cost-effective (US$ 0) for the case in which a saltmarsh was already present before and up to US$ 15 million (US $14–16 million) for the fully artificial saltmarsh restorations (Fig. 11a).

The implementation of nature-based measures would reduce the wave height by at least 1.6 m under the 500 yrs. return storm impacts. Thus, the wave barrier installed on top of the seawall could be removed. The reduced construction and maintenance cost of the hard seawall (Fig. 11a) was defined as the benefit of NBFD in the cost-benefit analysis (EQs. 5,6). We found NPV > 0 and BCR > 1 for all three measures, indicating a practical economic benefit over the long term (Fig. 11b, c). Notably, the NPV trend of the submerged breakwater (yellow line) and artificial saltmarsh (deep blue line) was upward, mainly due to the maintenance costs being reduced over time, while the timber pile (orange line) remained essentially unchanged due to the offset of their maintenance costs. Finally, after 38 years, the NPVs of timber pile(flat,tp), submerged breakwater(flat,sb), and wetland nourishment(flat,sn) were US$ 29 million, US$ 43 million, and US$ 36 million, with the benefit to cost ratios (BCRs) are 2.31, 6.32, and 3.49, respectively. Therefore, the submerged breakwater(flat,sb) was most cost-effective compared with artificial saltmarsh restoration(flat,sn) and timber piles(flat,tp) on CDS. Although the cost of natural saltmarsh was low, it would only become effective after the vegetation was totally recovered; therefore, would take longer time.

In addition, the cost and benefit of the equivalent wave attenuation between the summer vegetation on CDS and 0.4 m sedimentary nourishments
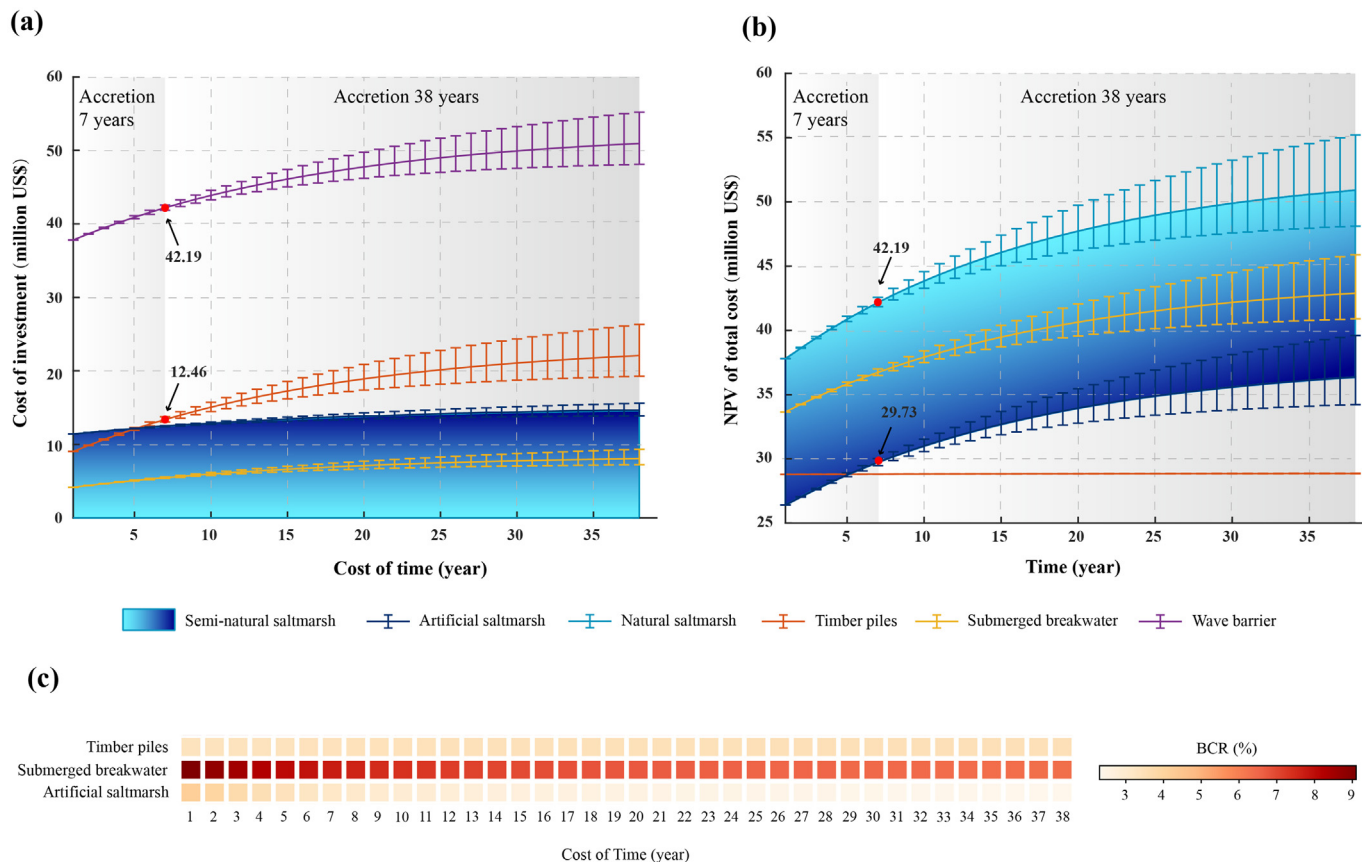
(a)

(b)

(c)

Fig. 11. Comparison of cost and benefit for NBFD measures. (a) The investment cost of natural saltmarsh, artificial saltmarsh, timber piles$_{(flat,tp)}$, submerged breakwater$_{(flat,sb)}$, and seawall wave barrier. (b) Total net present value (NPV) of costs and benefits for four NBFD measures. (c) The cost-benefit ratio (BCR) of the three NBFD measures. The darker the colour (when BCR > 1), the more cost-effective the measure. The results are based on a 6% discount rate, with the band indicating the 4% and 8% discount rate, respectively.

$_{(flat,sn)}$ were evaluated. The natural accretion of 0.4 m on CDS would take approximately seven years (Li et al.,2014). Although the sedimentary layer was more stable than the saltmarsh on wave mitigation as discussed above, the seven-year rapid natural accretion was only possible with the help of vegetation trapping. Notably, for the saltmarsh-based measures, the natural saltmarsh was the most cost-effective because saltmarsh was self-maintaining; the artificial saltmarsh was costly, high up to US$ 12 million (US$ 12–13 million); the semi-natural saltmarsh restoration varied in between (Fig. 11a). Comparatively, the most cost-effective measure was the construction of a submerged breakwater (Fig. 11c), which additionally created a wave-free zone on the tidal flat, fostering a suitable habitat for saltmarsh establishment and forming positive feedback for deposition.

5. Discussion

Nature-based climate change adaptions, such as the coastal wetland and saltmarsh, meet the long-term interests of human welfare (Temmerman et al., 2013; Vuik et al., 2019; Marijnissen et al., 2020; Willemsen et al., 2020). Most studies have focused on the above-ground vegetation structure for wave attenuations (Nowacki et al., 2017; Baron-Hyppolite et al., 2019; Garzon et al., 2019; Chong et al., 2021). However, the function of the underlying saltmarsh morphology is underestimated (Vuik et al., 2019). Besides, the stability of vegetation above-ground structure is challenged due to the vulnerability of stems and leaves during storm impacts (Vuik et al., 2018a, 2018b). We argue that the value of saltmarsh sedimentary layer, formed by sediment deposition due to vegetation trapping and consolidated by the root system, is more stable and effective in attenuating waves. In this paper, the simulation of wave attenuation by saltmarsh morphology and saltmarsh vegetation have been compared under designed return levels of

storm impacts on CDS, i.e., in the subtropical zone, where the saltmarsh withered in winter. We emphasize the added-value of saltmarsh sedimentary layer, which is continuously accreted by saltmarsh vegetation, especially during the flourishing season, potentially reducing the uncertainty of NBFD for coastal safety even during the winter, thereby reducing doubts about saltmarsh-based coastal protection in heavily urbanized coastal areas.

5.1. The value of saltmarsh morphology for coastal protection

Wave propagation to the coastal area is restricted by the shallow waters (Vuik et al., 2016), which reduces wave heights with the increasing of foreshore width (Fig. 9) and the thickening of sedimentary layer (Fig. 6g,h,i). We demonstrated a more effective function of saltmarsh morphology compared to the above-ground saltmarsh vegetation on wave attenuation, especially under severe storm impact (Figs. 7,8,9). Even for the narrow tidal flats on the south part of CDS, the wave attenuations benefit from the thick sedimentary layer (Fig. 7). The sedimentary layer of the coastal saltmarsh is much more stable than the above-ground vegetation structure, which is often regarded as fragile in the conventional NBFD study (Bouma et al., 2014). Stems of saltmarsh are easily broken by severe storm waves, usually taking 3–5 years to fully recover in natural conditions (Foster et al., 2013). In contrast, a mudflat surface disturbed by severe storms tends to recover within one week, at most 1–2 months even for 10-20 cm deep erosion (Leonardi et al., 2018), substantially reducing the uncertainties in defense for successive storm impacts. Moreover, the root expansion of saltmarsh vegetation helps to consolidate the deposition and stabilize the soil (Leonardi et al., 2018). Previous studies have demonstrated that coastal saltmarsh adapts to sea-level rise by trapping sediments

(Kirwan et al., 2016; Vuik et al., 2019; Marijnissen et al., 2020). However, the fact that the annual sedimentation rate was smaller than the sea-level rise rate in sediment-starving estuaries (Vuik et al., 2019) potentially covers the role of intertidal morphology for saltmarsh-based flood defense (Willemsen et al., 2020).

In contrast, the Yangtze Estuary is a high SSC estuary (Liu et al., 2010; Li et al., 2014). Half of the river-borne sediments from upstream were deposited in the estuary due to flow diffusion, and the rest spread to the sea, but some parts were transported back by flood tide (Dai et al., 2015). The coastal saltmarsh is the nature of sediment sink (Temmerman et al., 2013). Without considering storm disturbances, the sediments brought by tides could accrete 60 mm/yr on the CDS (Li et al., 2014), much higher than the current sea level rise rate 3.6 mm/yr (Oppenheimer et al., 2019). When the vertical sedimentation increase is limited by the tidal range (high tide level is approximately ~2.5 m), the thickening process is converted to transgressive deposition. Consequently, the expanding speed of CDS was measured to be 150 m/yr to the eastward before the construction of the Three Gorges dam (Ma et al., 2004). When storm surge superposition with high spring tide often results in extreme high-water levels, the energetic waves tend to erode the intertidal and subtidal morphology (Leonardi et al., 2018). This means that constructing wave-reducing structures (e.g., submerged breakwaters) at low water boundaries is most effective in breaking waves and reducing tidal flat erosion (Fig. 6). The reduced wave shear stress behind the breakwater protects the saltmarsh even during storms, helping the saltmarsh morphology recover quickly during the non-storm period. In contrast, in a low SSC environment, artificial sand nourishment is necessary to provide sediment sources, such as the coastal restoration works in the Pearl River Estuary (Lee and Khim, 2017). The advantage of the high SSC estuary is to guarantee a high natural deposition rate, hence reducing the cost of maintaining the saltmarsh. In the future, we believe that the role of the saltmarsh sedimentary layer will be more important on coastal protection in the context of global climate changes, especially for the accretional estuaries.

5.2. Sensitivity test of vegetation modelling and vegetation setting on wave attenuation

Two numerical methods were tested to examine the reliability of the employed vegetation modelling approaches on discerning the relative importance of saltmarsh morphology and saltmarsh vegetation on wave attenuation, i.e., the implicit versus explicit vegetation modellings. The explicit vegetation modelling simulates the 3D-disturbance effect of vegetation on wave dissipation based on the source term and convective flux calculation, which takes the effects of more complex processes occurring throughout the water column (Perthame and Simeoni, 2001; Mentaschi et al., 2018). In contrast, the implicit vegetation modelling simplifies the 3D-vegetation dissipation effect employing enhanced Nikuradse roughnesses (Vuik et al., 2016). The main difference between the two approaches is the location of saltmarsh where the role of depth-induced wave breaking plays. By excluding the influence of the various vegetation properties on wave attenuation (implicit modelling), waves retained more energy further shoreward, resulting in intense depth-induced wave breaking on the high intertidal zone. In contrast, with the explicit vegetation modelling, the waves experience significant attenuation at the vegetation front edge through intense wave-cylinder interactions, such that the breaking criteria (ratio of breaking wave height to water depth) are not violated at nearshore. Similar results were also observed in the explicit vegetation modelling using the bulk drag force approach (in terms of C_D values) by Baron-Hyppolite et al. (2019) and Nowacki et al. (2017) when comparing with the conventional bottom roughness modelling. However, treating vegetation as enhanced bottom roughness or the bulk drag force approach under-represents the detailed vegetation turbulence in monomer (Fig. 10c). Along with general performance, the total work done by both vegetation modelling approaches was similar after calibration. The two vegetation modelling approaches produced different wave dissipation mechanisms can be very important when considering the morphological stability of the marsh (Nowacki et al., 2017; Baron-Hyppolite et al., 2019).

A special exponential wave energy dissipation for a single vegetation setup and a linear wave energy dissipation for the mixed vegetation setup was found on the CDS (Fig. 9). Some researchers argue that exponential energy dissipation (uniform work) can achieve the minimum entropy production (or maximum entropy), which is the most stable state according to the principle of the second law of thermodynamics (Leopold and Langbein, 1962; Glansdorff and Prigogine, 1970). However, the natural condition of vegetation on CDS is mixed with *P. australis* and *S. mariqueter*, which is the actual condition by natural selection for wave dissipation. In the mixed vegetation setting, the *S. mariqueter* grows on the low-medium intertidal zone, and the *P. australis* grows on the high intertidal zone. Although the wave dissipation rate of *S. mariqueter* is only 5–12%, which is about half of the dissipation capacity of *P. australis* (Fig. 7), *S. mariqueter* is less likely to break due to the toughness of the stem (Willemsen et al., 2020). Thus, *S. mariqueter* on the low intertidal zone is more effective in storm wave resilience by preventing strong depth-induced wave breaking, therefore protecting the low intertidal morphology from erosion (Vuik et al., 2016; Willemsen et al., 2020). If the tall vegetation of *P. australis* was planted on the low intertidal zone (the single vegetation scenario), a tremendous amount of wave energy was dissipated (Fig. 7c). When encountering the upcoming wave will result in strong erosion of the tidal front due to the rapid wave energy release. A similar erosion mechanism also occurred for the high-narrow tidal flat, where cliffs were found in front of the bare tidal flat (Vuik et al., 2019). Therefore, we argue that uniform wave dissipation of the mixed vegetation setting is a more stable way of energy dissipation on CDS. Similar conclusions of uniform energy dissipation are also obtained by Van der Wegen et al. (2008) for the long-term evolution of alluvial estuaries. Notably, the zonal vegetation distribution on the tidal flat is determined by the periodical tide inundation (Bouma et al., 2014). Since tidal range varies worldwide, the saltmarsh-based coastal protection should be adapted to the local condition of tidal hydrodynamics.

5.3. Which NBFD measure is the most cost-effective for coastal protection?

A big challenge for flood protection in the heavily urbanized coastal area is with limited space for constructing the flood mitigation measure. Seawalls are considered an effective measure for conventional coastal protection design but are regarded as unsustainable in the long run (Temmerman et al., 2013). To remedy the defect, building seawall with nature, which meets the same flood protection standard with reduced construction cost, is considered the benefit of NBFD measures. In addition, the ecosystem service of NBFD brings more important social benefits, e.g., water purification, habitation, tourism, and environmental restoration (Vuik et al., 2016; Morris et al., 2018). According to Vuik et al. (2019), the four criteria for strategy selection are cost-benefit, maintenance sustainability, habitat impact during initial construction, and extra value of long-term ecosystem service. Here, we also consider if the measure can serve the sedimentary layer accretions (Fig. 12). In general, the submerged breakwater is an attractive measure for CDS. Not only because it has lower cost for the initial building, but also has lower impact on the ecosystem and helps trap suspended sediment. In addition, the wave-free zone behind the breakwater further increases the chance of vegetation establishment, fostering a beneficent cycle. By contrast, the benefit of the timber piles is not as outstanding on the CDS (Fig. 12). However, the thick stems are very effective in trapping suspended sediments and sequestrating carbon, like mangroves living in the tropical coastal area (Das and Vincent, 2009; Koch et al., 2009). The large-scale timber pile field may also provide a basis for installing photovoltaic energy panels, which are attractive in the future for clean energy production (Wu et al., 2019). Sand nourishment is popular for wealthy coastal communities. In the United States, beach nourishment projects accounted for 80% of the total coastal protection projects in the 1990s, valued at US$ 5 million/km^2 for storm surge mitigation (Foster et al., 2013). Natural saltmarsh is an attractive NBFD measure. However, it is quite dependent on natural habitats. The artificial or semi-natural saltmarsh is expensive on initial construction, but the long-term benefits are substantial (Fig.11b blue surface).

Positive	Timber piles	Submerged breakwater	Sand nourishment	Natural saltmarsh
Neutral				
Negative				
Capacity of sediment capture				
Cost-effectiveness				
Initial ecological impact				
Required maintenance				

Fig. 12. Scaled indicators of tested measures for strategic selecting of coastal restorations.

CDS wetland is rich in external sediment supplies, but the Yangtze riverborne sediment had reduced by 60–70% after closing the Three Gorges Dams in 2003 (Dai et al., 2015). Although CDS is still under accretion, engineering interventions are necessary to preserve a wide saltmarsh, especially on the south coastline where some sections had experienced erosion (Gao, 2020). Moreover, there is limited coastal space available for saltmarsh in cities, especially in some heavily urbanized megacities (e.g., Shanghai, Tokyo, and New York City), where decision-makers favor conventional seawalls due to their high efficiency and space-saving (Temmerman et al., 2013; Oppenheimer et al., 2019). By contrast, some statements advise a complete restoration of the natural coastline since hard seawalls break the balance of the original ecology (Gao, 2020). However, the coastal area with a small fraction of terrestrial area produced at least half of the world's GDP (Hallegatte et al., 2013). Therefore, we advise a "golden mean" approach, e.g., building seawalls with nature by combining conventional seawalls with vegetated foreshores and nearshore submerged breakwater as a trinity model of NBFD measure (Fig. 13). The functions of the three components act dependently using the divide-and-conquer strategy, i.e., the breakwater is to reduce nearshore waves and intercept suspended sediments; the vegetated foreshore attenuates wave and consolidates saltmarsh morphology; the conventional seawall is lowered to only prevent extreme tidal levels and to limit wave overtopping. Such a compact system enlightened further application of NBFD to space-limited coastal cities.

5.4. Implications for coastal management

Future sea-level rise and storm strengthening are inevitable, which requires sustainable coastal management (Schuerch et al., 2019). Building seawalls with nature remedies the limitations of conventional hard seawall defense, particularly in estuarine deltas, where population exposure is high and sediment supplies are usually rich. However, an important bottleneck challenge that hinders the broad application of saltmarsh-based flood

defense is the uncertainty of vegetation stems and leaves on wave dissipation. We argue that the gradual sediment trapping and stabilization by vegetation and the root system, which raise the saltmarsh morphology, can effectively reduce the uncertainty of NBFD. Such morphologic wave attenuation process is based on the solid physical law of breaking wave height to the water depth ratio (Vuik et al., 2016). In sediment starving estuaries and coastlines, erosion of adjacent tidal flats can provide a local sediment source for saltmarsh accretion (Schuerch et al., 2019). Even along erosional coastline seems to weaken the advantage of morphologic wave attenuation, such as the transgressions observed in south China, the Wadden Sea, and Barnegat Bay in the USA (Temmerman et al., 2013; Leonardi et al., 2016). Nevertheless, proper artificial NBFD interventions, e.g., groins and oyster reefs (Temmerman et al., 2013; Vuik et al., 2019), can restrain erosion and restore the tidal flat. The equivalent sediment trapping ability by engineering measures and saltmarsh both serve the formation of a thick sedimentary layer. Additionally, saltmarsh and mangroves are important sinks of atmospheric CO_2, contributing to climate change adaptions (Duarte et al., 2013). We argue that nature-based flood defense design using the function of saltmarsh morphology fulfills sustainable coastal management. The promotion of this idea will facilitate joint research between ecologists and engineers and provoke governments and policy makers to support a broader application of NBFD.

6. Conclusions

The vulnerability of saltmarsh plants, especially the biological instability during storms, resulting in uncertainties in coastal protection, is considered an urgent challenge that hinders the development of NBFD. We demonstrated an important mechanism of coastal protection using the morphology of the coupled tidal flat – saltmarsh system, which was largely underestimated in previous studies. The positive feedback between saltmarsh and accretion, which increases and stabilizes the sedimentary layer in the long run, provides significant value on coastal protection. The
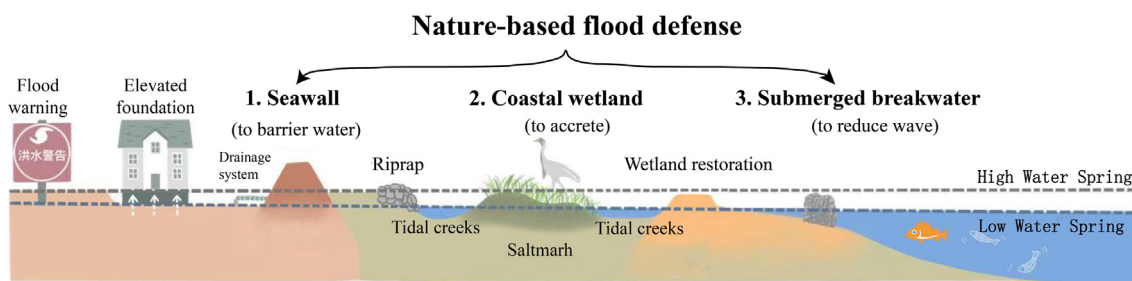

Fig. 13. A representative profile showing building seawall with nature concept by a combination of nearshore submerged breakwater-coastal saltmarsh-seawall as a trinity model of NBFD measure.

main findings are as follows. (1) Compared with the vulnerable vegetation above-ground structure, the foreshore morphology is more reliable and efficient on wave attenuation during storm conditions. (2) For vegetation type selection, *S.mariqueter* is less effective on wave attenuations than *P. australis* when stem breakage is neglected, but the soft and resilient stems of *S.mariqueter* are very effective in protecting the low tidal flat from erosion. (3) Sensitivity test showed that the Nikuradse roughnesses method used in the numerical modelling neglected the vertically and horizontally varied drag forces across the marsh, nevertheless, it is simple and effective in computing the relative contribution of vegetation and morphology on wave mitigation. (4) Artificial interventions of NBFD measures, such as sand nourishment, submerged breakwater, and timber piles, are effective in coastal protection based on the role of morphological wave attenuation. The submerged breakwater is attractive for CDS, high on the cost-benefit ratio (BCR), and brings an extra benefit in fostering coastal saltmarsh. We suggest building the hybrid coastal flood defense system, by a combination of conventional hard seawall with the submerged breakwater at offshore and vegetated foreshore in between based on a divide-and-conquer strategy. In general, for accreting coastlines, a positive feedback mechanism between saltmarsh and accretion contributes to sustainable coastal protection. Even in the erosive coastlines, geomorphology-based coastal protection can still be applied with human interventions. The demonstration of coastal protection using a saltmarsh-based morphological wave attenuation mechanism can substantially reduce the uncertainty for building NBFD and shed light on designing a reliable hybrid NBFD.

CRediT authorship contribution statement

Jie Mi: Data curation; Formal analysis; Investigation; Methodology; Writing
Min Zhang: Data curation; Formal analysis; Funding acquisition; Methodology; Investigation; Project administration; Writing
Zhenchang Zhu: Conceptualization; Investigation; Review & editing
Vincent Vuik: Formal analysis; Investigation; Methodology
Jiahong Wen: Data curation; Formal analysis; Software
Hongkai Gao: Review & editing
Tjeerd J. Bouma: Conceptualization; Review & editing

Appendix A

The most suitable probability density functions (PDFs) of the extreme monthly tidal level, storm surge, SWHs, and wave periods were selected by fitting to appropriate marginal distributions, i.e., Normal, Gamma, Weibull, and generalized extreme value (GEV). Statistics of the Chi-Square test for the theoretical marginal distributions resulted in the best choice of Gumbel for the tide, Gamma for the surge, and GEV for the SWHs and peak wave periods at the offshore boundary, respectively (Fig. A1).
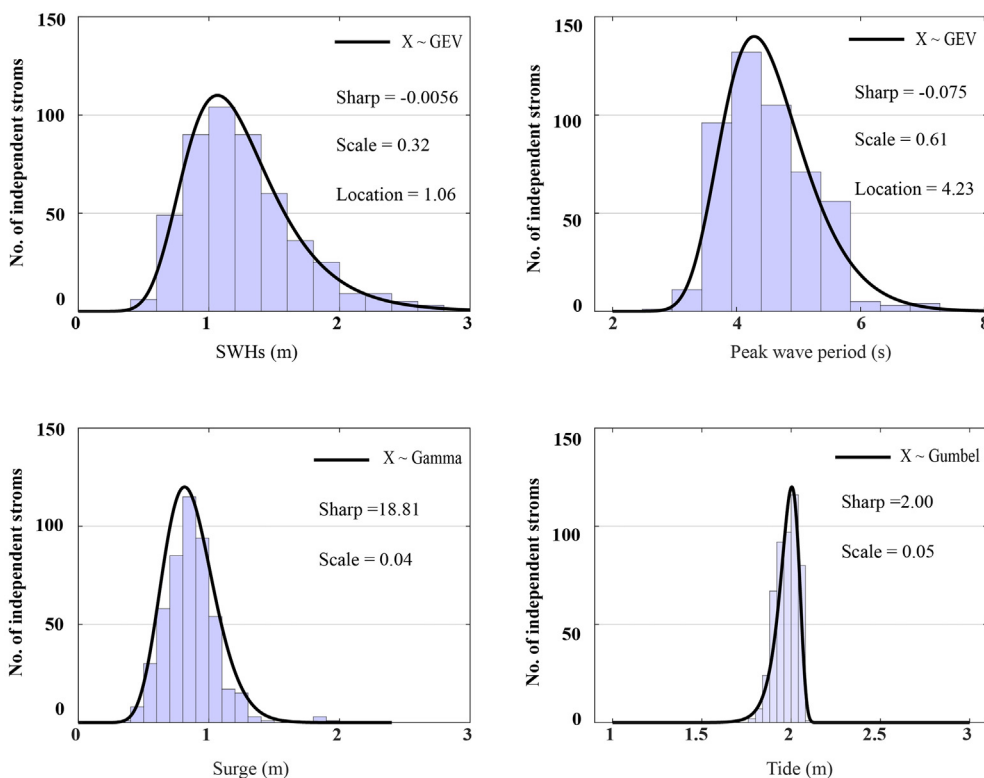

Fig. A1. The best-selecting of the probability density distribution function fitting to the hydrological boundary condition of the significant wave heights, peak wave periods, storm surges, and tidal levels.
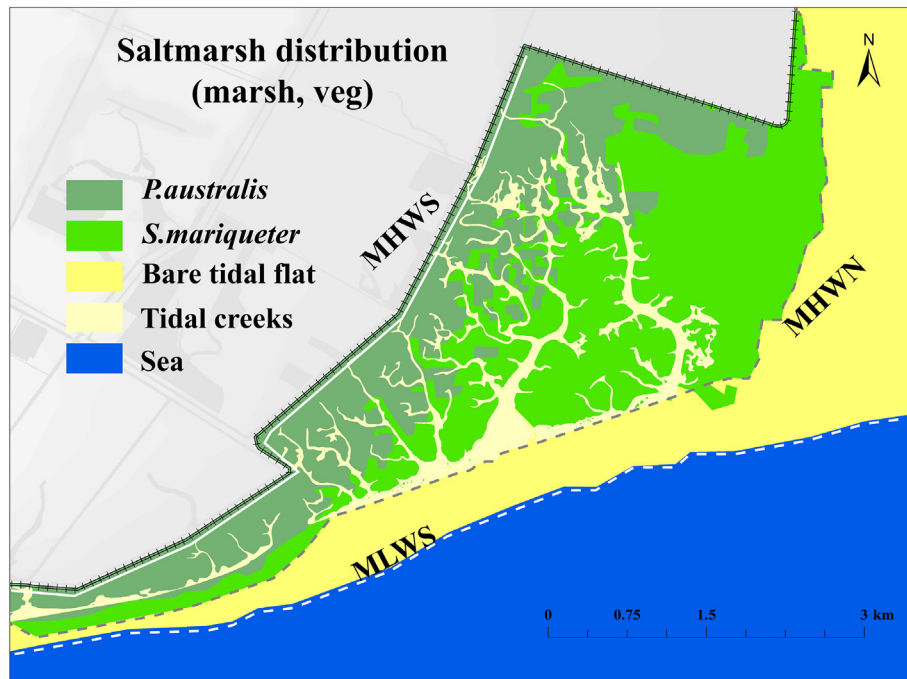
Fig. A2. The interpreted vegetation species and spatial distributions on Chongming Dongtan Shoal based on classification of Landsat8 image obtained on 19 November 2014.
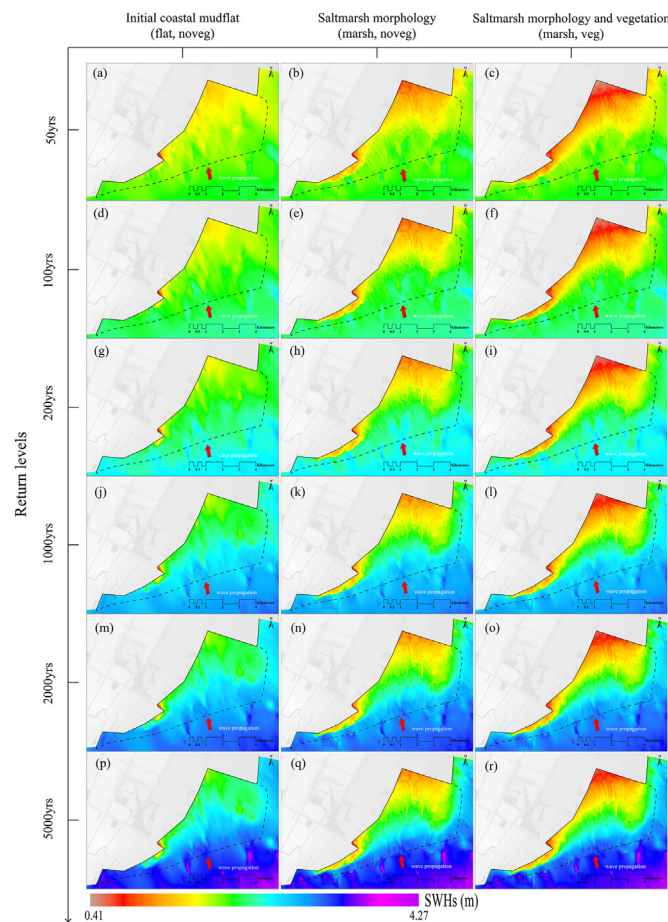

Fig. A3. Results of wave attenuations by Nature-Based Flood Defense (NBFD) under 50 yrs., 100 yrs., 200 yrs., 1000 yrs., 2000 yrs., and 5000 yrs. return hydrodynamic boundary conditions.

Table A1

List of net present value (NPV) and cost-benefit ratio (BCR) of the applied natural and nature-based solutions.

	Years	Natural saltmarsh	Semi-natural saltmarsh	Artificial saltmarsh	Timber piles	Submerged breakwater	Sand nourishment
NPV	0	37.80	26.41–37.80	26.41	28.78	33.65	−12.59
	7	42.19 (41.85–42.57)	29.73(29.47–30.02)-42.19(41.85–42.57)	29.73 (29.47–30.02)	28.81 (28.80–28.81)	36.73 (36.49–37.00)	−15.22 (−15.19–15.45)
	10	43.87 (43.27–44.56)	31.01(30.56–31.53)- 43.87(43.27–44.56)	31.01 (30.56–31.53)	28.82 (28.81–28.82)	37.92 (37.49–38.40)	−16.23 (−15.87–16.64)
	20	47.75 (46.21–49.74)	33.96(32.78–35.46)- 47.75(46.21–49.74)	33.96 (32.78–35.46)	28.84 (28.83–28.85)	40.64 (39.56–42.04)	−18.56 (−17.63–19.75)
	38	50.94 (48.11–55.20)	36.37(34.23–39.61)- 50.94(48.11–55.20)	36.37 (34.23–39.61)	28.86 (28.84–28.88)	42.89 (40.90–45.88)	−20.47 (−18.77–23.02)
BCR	0			3.32	4.19	9.10	0.75
	7			3.39 (3.38–3.39)	3.15 (3.21–3.09)	7.73 (7.82–7.52)	0.73 (0.74–0.73)
	10			3.41 (3.40–3.42)	2.19 (2.99–2.83)	7.37 (7.49–7.02)	0.73 (0.73–0.73)
	20			3.46 (3.44–3.48)	2.52 (2.66–2.38)	6.72 (6.95–6.00)	0.72 (0.72–0.72)
	38			3.50 (3.46–3.54)	2.31 (2.50–2.10)	6.32 (5.16–6.67)	0.71 (0.72–0.71)

References

Baron-Hyppolite, C., Lashley, C.H., Garzon, J., Miesse, T., Ferreira, C., Bricker, J.D., 2019. Comparison of implicit and explicit vegetation representations in SWAN hindcasting wave dissipation by coastal wetlands in Chesapeake Bay. Geosciences (Switzerland) 9 (1), 8. https://doi.org/10.3390/geosciences9010008.

Battjes, J., Janssen, H., 1978. Energy loss and set-up due to breaking random waves. Proc. 16th Conf. Coastal Engineering. vol. 1. ASCE, pp. 569–587. https://doi.org/10.9753/icce.v16.

Bouma, T.J., van Belzen, J., Balke, T., Zhu, Z., Airoldi, L., Blight, A.J., Davies, A.J., Galvan, C., Hawkins, S.J., Hoggart, S.P.G., Lara, J.L., Losada, I.J., Maza, M., Ondiviela, B., Skov, M.W., Strain, E.M., Thompson, R.C., Yang, S., Zanuttigh, B., Zhang, L., Herman, P.M.J., 2014. Identifying knowledge gaps hampering application of intertidal habitats in coastal protection: opportunities & steps to take. Coast. Eng. 87, 147–157. https://doi.org/10.1016/j.coastaleng.2013.11.014.

Chen, Q., Li, Y., Kelly, D.M., Zhang, K., Zachry, B., Rhome, J., 2021. Improved modeling of the role of mangroves in storm surge attenuation. Estuar. Coast. Shelf Sci. 260, 107515. https://doi.org/10.1016/j.ecss.2021.107515.

Cheng, L., AghaKouchak, A., Gilleland, E., Katz, R.W., 2014. Non-stationary extreme value analysis in a changing climate. Clim. Chang. 127 (2), 353–369. https://doi.org/10.1007/s10584-014-1254-5.

Chong, Z.T., Zhang, M., Wen, J.H., Wang, L.Y., Mi, J., Bricker, J., Nmor, S., Dai, Z.J., 2021. Coastal protection using building with nature concept: a case study from Chongming Dongtan Shoal, China. Acta Oceanol. Sin. 40 (11), 1–15. https://doi.org/10.1007/s13131-021-1761-y.

Dai, Z., Liu, J.T., Wei, W., Chen, J., 2015. Detection of the Three Gorges Dam influence on the Changjiang (Yangtze River) submerged delta. Sci. Rep.-UK 4 (1). https://doi.org/10.1038/srep06600.

Dai, Z., Fagherazzi, S., Mei, X., Gao, J., 2016. Decline in suspended sediment concentration delivered by the Changjiang (Yangtze) River into the East China Sea between 1956 and 2013. Geomorphology 268, 123–132. https://doi.org/10.1016/j.geomorph.2016.06.009.

Dai, Z., Fagherazzi, S., Mei, X., Chen, J., Meng, Y., 2016. Linking the infilling of the North Branch in the Changjiang (Yangtze) estuary to anthropogenic activities from 1958 to 2013. Mar. Geol. 379, 1–12. https://doi.org/10.1016/j.margeo.2016.05.006.

Dai, Z., Mei, X., Darby, S.E., Lou, Y., Li, W., 2018. Fluvial sediment transfer in the Changjiang (Yangtze) river-estuary depositional system. J. Hydrol. 566, 719–734. https://doi.org/10.1016/j.jhydrol.2018.09.019.

Dalrymple, R.A., Kirby, J.T., Hwang, P.A., 1984. Wave diffraction due to areas of energy dissipation. J. Waterw. Port, CoastOcean Eng. 110 (1), 67–79. https://doi.org/10.1061/(ASCE)0733-950X(1984)110:1(67).

Das, S., Vincent, J.R., 2009. Mangroves protected villages and reduced death toll during Indian super cyclone. Proc. Natl. Acad. Sci. U. S. A. 106 (18), 7357–7360. https://doi.org/10.1073/pnas.0810440106.

Dee, D.P., Uppala, S.M., Simmons, A.J., Berrisford, P., Poli, P., Kobayashi, S., Andrae, U., Balmaseda, M.A., Balsamo, G., Bauer, P., Bechtold, P., Beljaars, A.C.M., van de Berg, L., Bidlot, J., Bormann, N., Delsol, C., Dragani, R., Fuentes, M., Geer, A.J., Haimberger, L., Healy, S.B., Hersbach, H., Hólm, E.V., Isaksen, L., Kållberg, P., Köhler, M., Matricardi, M., Mcnally, A.P., Monge-Sanz, B.M., Morcrette, J.J., Park, B.K., Peubey, C., de Rosnay, P., Tavolato, C., Thépaut, J.N., Vitart, F., 2011. The ERA-Interim reanalysis: configuration and performance of the data assimilation system. Q. J. R. Meteorol. Soc. 137 (656), 553–597. https://doi.org/10.1002/qj.828.

Duarte, C.M., Losada, I.J., Hendriks, I.E., Mazarrasa, I., Marbà, N., 2013. The role of coastal plant communities for climate change mitigation and adaptation. Nat. Clim. Chang. 3 (11), 961–968. https://doi.org/10.1038/nclimate1970.

Egbert, G.D., Erofeeva, S.Y., 2002. Efficient inverse modeling of barotropic ocean tides. J. Atmos. Ocean. Technol. 19 (2), 183–204. https://doi.org/10.1175/1520-0426(2002)019<0183:EIMOBO>2.0.CO;2.

Egbert, G.D., Bennett, A.F., Foreman, M.G.G., 1994. TOPEX/POSEIDON tides estimated using a global inverse model. J. Geophys. Res. Oceans 99 (C12), 24821–24852. https://doi.org/10.1029/94JC01894.

Foster, N.M., Hudson, M.D., Bray, S., Nicholls, R.J., 2013. Intertidal mudflat and saltmarsh conservation and sustainable use in the UK: a review. J. Environ. Manag. 126, 96–104. https://doi.org/10.1016/j.jenvman.2013.04.015.

Gao, S., 2020. Green seawall blueprint to prevent future storm surge disasters. Sci. 72 (04), 12–16 (in Chinese with English abstract).

Garzon, J.L., Maza, M., Ferreira, C.M., Lara, J.L., Losada, I.J., 2019. Wave attenuation bySpartina saltmarshes in the Chesapeake bay under storm surge conditions. J. Geophys. Res. Oceans 124 (7), 5220–5243. https://doi.org/10.1029/2018JC014865.

Gijón Mancheño, A., Jansen, W., Uijttewaal, W.S.J., Reniers, A.J.H.M., van Rooijen, A.A., Suzuki, T., Etminan, V., Winterwerp, J.C., 2021. Wave transmission and drag coefficients through dense cylinder arrays: implications for designing structures for mangrove restoration. Ecol. Eng. 165, 106231. https://doi.org/10.1016/j.ecoleng.2021.106231.

Glansdorff, P., Prigogine, I., 1970. Non-equilibrium stability theory. Physica 46 (3), 344–366. https://doi.org/10.1016/0031-8914(70)90010-8.

Hallegatte, S., Green, C., Nicholls, R.J., Corfee-Morlot, J., 2013. Future flood losses in major coastal cities. Nat. Clim. Chang. 3 (9), 802–806. https://doi.org/10.1038/nclimate1979.

Hu, Z., Ge, Z., Ma, Q., Zhang, Z., Tang, C., Cao, H., Zhang, T., Li, B., Zhang, L., 2015. Revegetation of a native species in a newly formed tidal marsh under varying hydrological conditions and planting densities in the Yangtze Estuary. Ecol. Eng. 83, 354–363. https://doi.org/10.1016/j.ecoleng.2015.07.005.

Kang, Y., Ding, X., Xu, F., Zhang, C., Ge, X., 2017. Topographic mapping on large-scale tidal flats with an iterative approach on the waterline method. Estuar. Coast. Shelf Sci. 190, 11–22. https://doi.org/10.1016/j.ecss.2017.03.024.

Kirwan, M.L., Temmerman, S., Skeehan, E.E., Guntenspergen, G.R., Fagherazzi, S., 2016. Overestimation of marsh vulnerability to sea level rise. Nat. Clim. Chang. 6 (3), 253–260. https://doi.org/10.1038/nclimate2909.

Koch, E.W., Barbier, E.B., Silliman, B.R., Reed, D.J., Perillo, G.M., Hacker, S.D., Granek, E.F., Primavera, J.H., Muthiga, N., Polasky, S., Halpern, B.S., Kennedy, C.J., Kappel, C.V., Wolanski, E., 2009. Non-linearity in ecosystem services: temporal and spatial variability in coastal protection. Front. Ecol. Environ. 7 (1), 29–37. https://doi.org/10.1890/080126.

Lee, S.Y., Khim, J.S., 2017. Hard science is essential to restoring soft-sediment intertidal habitats in burgeoning East Asia. Chemosphere 168, 765–776. https://doi.org/10.1016/j.chemosphere.2016.10.136.

Leonardi, N., Defne, Z., Ganju, N., Fagherazzi, S., 2016. Salt marsh erosion rates and boundary features in a shallow bay: indicators salt marsh erosion New Jersey. J. Geophys. Res. Earth. Surf. https://doi.org/10.1002/2016JF003975.

Leonardi, N., Carnacina, I., Donatelli, C., Ganju, N.K., Plater, A.J., Schuerch, M., Temmerman, S., 2018. Dynamic interactions between coastal storms and salt marshes: a review. Geomorphology 301, 92–107. https://doi.org/10.1016/j.geomorph.2017.11.001.

Leopold, L.B., Langbein, W.B., 1962. The concept of entropy in landscape evolution. Professional Paper. U.S. Government Printing Office, Washington, D.C, pp. A1–A20 https://doi.org/10.3133/pp500A.

Li, X., Ren, L., Liu, Y., Craft, C., Mander, Ü., Yang, S., 2014. The impact of the change in vegetation structure on the ecological functions of salt marshes: the example of the Yangtze estuary. Reg. Environ. Chang. 14 (2), 623–632. https://doi.org/10.1007/s10113-013-0520-9.

Liu, H., He, Q., Wang, Z., Weltje, G.J., Zhang, J., 2010. Dynamics and spatial variability of near-bottom sediment exchange in the Yangtze Estuary,China. Estuar. Coast. Shelf Sci. 86 (3), 322–330. https://doi.org/10.1016/j.ecss.2009.04.020.

Ma, Z., Li, B., Zhao, B., Jing, K., Tang, S., Chen, J., 2004. Are artificial wetlands good alternatives to natural wetlands for waterbirds? – a case study on Chongming Island,China. Biodivers. Conserv. 13 (2), 333–350. https://doi.org/10.1023/B:BIOC.0000006502.96131.59.

Madsen, O.S., Poon, Y.-K., Graber, H.C., 1988. Spectral wave attenuation by bottom friction: theory. Proceedings of the 21st International Conference on Coastal Engineering, Malaga, Spain. American Society of Civil Engineers, New York, NY, USA, pp. 492–504.

Marijnissen, R., Esselink, P., Kok, M., Kroeze, C., van Loon-Steensma, J.M., 2020. How natural processes contribute to flood protection - a sustainable adaptation scheme for a wide green dike. Sci. Total Environ. 739, 139698. https://doi.org/10.1016/j.scitotenv.2020.139698.

Méndez, F.J., Losada, I.J., 2004. An empirical model to estimate the propagation of random breaking and nonbreaking waves over vegetation fields. Coast. Eng. 51 (2), 103–118. https://doi.org/10.1016/j.coastaleng.2003.11.003.

Méndez, F.J., Losada, I.J., Losada, M.A., 1999. Hydrodynamics induced by wind waves in a vegetation field. J. Geophys. Res. Oceans 104 (C8), 18383–18396. https://doi.org/10.1029/1999JC900119.

Mentaschi, L., Kakoulaki, G., Vousdoukas, M., Voukouvalas, E., Feyen, L., Besio, G., 2018. Parameterizing unresolved obstacles with source terms in wave modeling: a real-world application. Ocean Model 126, 77–84. https://doi.org/10.1016/j.ocemod.2018.04.003.

Möller, I., Spencer, T., 2002. Wave dissipation over macro-tidal saltmarshes: effects of marsh edge typology and vegetation change. J. Coast. Res. 36, 506–521. https://doi.org/10.2112/1551-5036-36.sp1.506.

Möller, I., Kudella, M., Rupprecht, F., Spencer, T., Paul, M., van Wesenbeeck, B.K., Wolters, G., Jensen, K., Bouma, T.J., Miranda-Lange, M., Schimmels, S., 2014. Wave attenuation over coastal salt marshes under storm surge conditions. Nat. Geosci. 7 (10), 727–731. https://doi.org/10.1038/ngeo2251.

Morris, R.L., Konlechner, T.M., Ghisalberti, M., Swearer, S.E., 2018. From grey to green: efficacy of eco-engineering solutions for nature-based coastal defence. Glob. Chang. Biol. 24 (5), 1827–1842. https://doi.org/10.1111/gcb.14063.

NFGAP, 2018. Construction standard of wetland protection project. The National Forestry and Grassland Administration of People's Republic of China. http://www.forestry.gov.cn/main/217/20180816/171258480891411.html/. (Accessed 20 March 2021).

Nowacki, D.J., Beudin, A., Ganju, N.K., 2017. Spectral wave dissipation by submerged aquatic vegetation in a back-barrier estuary. Limnol. Oceanogr. 62 (2), 736–753. https://doi.org/10.1002/lno.10456.

Oppenheimer, M., Glavovic, B.C., Hinkel, J., van de Wal, R., Magnan, A.K., Abd-Elgawad, A., Cai, R., Cifuentes-Jara, M., DeConto, R.M., Ghosh, T., Hay, J., Isla, F., Marzeion, B., Meyssignac, B., Sebesvari, Z., 2019. Sea level rise and implications for low-lying islands, coasts and communities. In: Pörtner, H.-O., Roberts, D.C., Masson-Delmotte, V., Zhai, P., Tignor, M., Poloczanska, E., Mintenbeck, K., Alegría, A., Nicolai, M., Okem, A., Petzold, J., Rama, B., Weyer, N.M. (Eds.), IPCC Special Report on the Ocean and Cryosphere in a Changing Climate.

Perthame, B., Simeoni, C., 2001. A kinetic scheme for the Saint-Venant system with a source term. Calcolo 38 (4), 201–231. https://doi.org/10.1007/s10092-001-8181-3.

Pinsky, M.L., Guannel, G., Arkema, K.K., 2013. Quantifying wave attenuation to inform coastal habitat conservation. Ecosphere 4 (8), t95. https://doi.org/10.1890/ES13-00080.1.

QMWS, 2019. Quota for maritime works in seaport. Ministry of Transport of the People's Republic of China. https://www.mot.gov.cn/. (Accessed 20 March 2021).

Reed, D., van Wesenbeeck, B., Herman, P.M.J., Meselhe, E., 2018. Tidal flat-wetland systems as flood defenses: understanding biogeomorphic controls. Estuar. Coast. Shelf Sci. 213, 269–282. https://doi.org/10.1016/j.ecss.2018.08.017.

Ruessink, B.G., Walstra, D.J.R., Southgate, H.N., 2003. Calibration and verification of a parametric wave model on barred beaches. Coast. Eng. 48 (3), 139–149. https://doi.org/10.1016/S0378-3839(03)00023-1.

Schuerch, M., Spencer, T., Temmerman, S., Kirwan, M.L., Wolff, C., Lincke, D., McOwen, C.J., Pickering, M.D., Reef, R., Vafeidis, A.T., Hinkel, J., Nicholls, R.J., Brown, S., 2019. Author correction: future response of global coastal wetlands to sea-level rise. Nature 569 (7757), E8. https://doi.org/10.1038/s41586-019-1205-4.

Spencer, T., Möller, I., Rupprecht, F., Bouma, T.J., van Wesenbeeck, B.K., Kudella, M., Paul, M., Jensen, K., Wolters, G., Miranda-Lange, M., Schimmels, S., 2016. Salt marsh surface survives true-to-scale simulated storm surges. Earth Surf. Proc. Land. 41 (4), 543–552. https://doi.org/10.1002/esp.3867.

Syvitski, J.P.M., Kettner, A.J., Overeem, I., Hutton, E.W.H., Hannon, M.T., Brakenridge, G.R., Day, J., Vörösmarty, C., Saito, Y., Giosan, L., Nicholls, R.J., 2009. Sinking deltas due to human activities. Nat. Geosci. 2 (10), 681–686. https://doi.org/10.1038/ngeo629.

Temmerman, S., Meire, P., Bouma, T.J., Herman, P.M.J., Ysebaert, T., De Vriend, H.J., 2013. Ecosystem-based coastal defence in the face of global change. Nature 504 (7478), 79–83. https://doi.org/10.1038/nature12859.

U.S. Geological Survey, 2016. Geological Survey Gap/Landfire National Terrestrial Ecosystems. U.S. Geological Survey, Reston, VA, USA.

Vuik, V., Jonkman, S.N., Borsje, B.W., Suzuki, T., 2016. Nature-based flood protection: the efficiency of vegetated foreshores for reducing wave loads on coastal dikes. Coast. Eng. 116, 42–56. https://doi.org/10.1016/j.coastaleng.2016.06.001.

Vuik, V., Suh Heo, H.Y., Zhu, Z., Borsje, B.W., Jonkman, S.N., 2018a. Stem breakage of salt marsh vegetation under wave forcing: a field and model study. Estuar. Coast. Shelf Sci. 200, 41–58. https://doi.org/10.1016/j.ecss.2017.09.028.

Vuik, V., van Vuren, S., Borsje, B.W., van Wesenbeeck, B.K., Jonkman, S.N., 2018b. Assessing safety of nature-based flood defenses: dealing with extremes and uncertainties. Coast. Eng. 139, 47–64. https://doi.org/10.1016/j.coastaleng.2018.05.002.

Vuik, V., Borsje, B.W., Willemsen, P.W.J.M., Jonkman, S.N., 2019. Salt marshes for flood risk reduction: quantifying long-term effectiveness and life-cycle costs. Ocean Coast. Manag. 171, 96–110. https://doi.org/10.1016/j.ocecoaman.2019.01.010.

van der Wegen, M., Wang, Z.B., Savenije, H.H.G., Roelvink, J.A., 2008. Long-term morphodynamic evolution and energy dissipation in a coastal plain, tidal embayment. J. Geophys. Res. 113 (F3). https://doi.org/10.1029/2007JF000898.

Willemsen, P.W.J.M., Borsje, B.W., Vuik, V., Bouma, T.J., Hulscher, S.J.M.H., 2020. Field-based decadal wave attenuating capacity of combined tidal flats and salt marshes. Coast. Eng. 156, 103628. https://doi.org/10.1016/j.coastaleng.2019.103628.

Wu, Y., Li, L., Song, Z., Lin, X., 2019. Risk assessment on offshore photovoltaic power generation projects in China based on a fuzzy analysis framework. J. Clean. Prod. 215, 46–62. https://doi.org/10.1016/j.jclepro.2019.01.024.

Wu, L.G., Zhao, H.K., Wang, C., Cao, J., Liang, J., 2022. Understanding of the effect of climate change on tropical cyclone intensity: a review. Adv. Atmos. Sci. 39 (2), 205–221. https://doi.org/10.1007/s00376-021-1026-x.

Yilmaz, C.S., Yilmaz, V., Gungor, O., 2018. Investigating the performances of commercial and non-commercial software for ground filtering of UAV-based point clouds. Int. J. Remote Sens. 39 (15–16), 5016–5042. https://doi.org/10.1080/01431161.2017.1420942.

Zhang, M., Townend, I., Zhou, Y., Cai, H., 2016. Seasonal variation of river and tide energy in the Yangtze estuary,China. Earth Surf. Proc. Land. 41 (1), 98–116. https://doi.org/10.1002/esp.3790.

Zhang, M., Townend, I., Cai, H., He, J., Mei, X., 2018. The influence of seasonal climate on the morphology of the mouth-bar in the Yangtze Estuary,China. Cont. Shelf Res. 153, 30–49. https://doi.org/10.1016/j.csr.2017.12.004.

Zhang, M., Dai, Z., Bouma, T.J., Bricker, J., Townend, I., Wen, J., Zhao, T., Cai, H., 2021. Tidal-flat reclamation aggravates potential risk from storm impacts. Coast. Eng. 166, 103868. https://doi.org/10.1016/j.coastaleng.2021.103868.

Zhou, Z., van der Wegen, M., Jagers, B., Coco, G., 2016. Modelling the role of self-weight consolidation on the morphodynamics of accretional mudflats. Environ. Model. Softw. 76, 167–181. https://doi.org/10.1016/j.envsoft.2015.11.002.

Zhu, Z., Vuik, V., Visser, P.J., Soens, T., van Wesenbeeck, B., van de Koppel, J., Jonkman, S.N., Temmerman, S., Bouma, T.J., 2020. Historic storms and the hidden value of coastal wetlands for nature-based flood defence. Nat. Sustain. 3 (10), 853–862. https://doi.org/10.1038/s41893-020-0556-z.